
Environmental Fluid Mechanics **4:** 1–56, 2004.

Integral Model for Turbulent Buoyant Jets in Unbounded Stratified Flows. Part I: Single Round Jet

GERHARD H. JIRKA
Institute for Hydromechanics, University of Karlsruhe, Karlsruhe, Germany

Received 13 January 2003; accepted in revised form 6 April 2003

Abstract. The mechanics of buoyant jet flows issuing with a general three-dimensional geometry into an unbounded ambient environment with uniform density or stable density stratification and under stagnant or steady sheared current conditions is investigated. An integral model is formulated for the conservation of mass, momentum, buoyancy and scalar quantities in the turbulent jet flow. The model employs an entrainment closure approach that distinguishes between the separate contributions of transverse shear (leading to jet, plume, or wake internal flow dynamics) and of azimuthal shear mechanisms (leading to advected momentum puff or thermal flow dynamics), respectively. Furthermore, it contains a quadratic law turbulent drag force mechanism as suggested by a number of recent detailed experimental investigations on the dynamics of transverse jets into crossflow. The model is validated in several stages: First, comparison with basic experimental data for the five asymptotic, self-similar stages of buoyant jet flows, i.e., the pure jet, the pure plume, the pure wake, the advected line puff, and the advected line thermal, support the choice and magnitude of the turbulent closure coefficients contained in the entrainment formulation. Second, comparison with many types of non-equilibrium flows support the proposed transition function within the entrainment relationship, and also the role of the drag force in the jet deflection dynamics. Third, a number of spatial limits of applicability have been proposed beyond which the integral model necessarily becomes invalid due to its parabolic formulation. These conditions, often related to the breakdown of the boundary layer nature of the flow, describe features such as terminal layer formation in stratification, upstream penetration in jets opposing a current, or transition to passive diffusion in a turbulent ambient shear flow. Based on all these comparisons, that include parameters such as trajectories, centerline velocities, concentrations and dilutions, the model appears to provide an accurate and reliable representation of buoyant jet physics under highly general flow conditions.

1. Introduction and Historical Perspective

A buoyant jet is the fluid motion caused by the sustained injection of fluid momentum and buoyancy through an orifice into an ambient receiving fluid body and gradually evolving along a trajectory within that receiving fluid. The buoyant jet flow is fully turbulent whenever its efflux Reynolds number, based on efflux velocity, orifice dimension and fluid kinematic viscosity, is sufficiently large (greater than about 10^3).

Buoyant jet motions (sometimes called forced plumes) are prevalent in the natural environment and in engineering applications. They are most spectacular in volcanic gas eruptions, they occur as hydrothermal vent flows in the deep ocean or as fresh groundwater plumes in the coastal zone. They are a key feature in society's fluid waste disposal methods, be it in the form of gaseous emissions into the atmosphere from industrial and domestic smokestacks, from mobile exhausts and from cooling towers, or of liquid releases into water bodies from industrial, municipal and agricultural sources or mining and oil extraction operations. They are an integral part of building ventilation and air conditioning systems. And they play a central role as mixing and injection devices in chemical reactors, waste and sewage treatment plants, desalination plants, combustion chambers, jet engines, or heat exchangers as well as stratification control and oxygenation devices in lakes or reservoirs.

Depending on the source and ambient flow interaction in the above instances many complexities and a rich variety of flow phenomena can take place in buoyant jet flows. This is reflected in the vast and diverse amount of literature that exists on this topic.

The source fluxes can be steady or time variable in form of starting or of pulsating flows. The momentum flux may have a simple forward component, or a swirling motion may be superposed. The buoyancy agent in the source flow relative to the ambient may be caused by a variety of effects: The inflow may differ in its heat content or due to in-phase admixtures or solutions (such as other gases for atmospheric emissions, dissolved solids or other miscible liquids for aqueous releases) or due to out-of-phase admixtures (such as solid particles, liquid droplets in gases, gas bubbles or immiscible fluids in liquids). Finally, the efflux geometry can be a simple round pipe, port or nozzle, or orifices of more general cross-sections (including the two-dimensional plane or slot jet) or multiple orifices (multiport diffusers) with many different alignment and orientation possibilities.

As for the receiving fluid body, it is characterized by its density field, its velocity field and its overall geometry. The ambient may be of uniform density, it may contain a stable density stratification – a decreasing density (or potential density for compressible fluids) with increasing elevation – or may exhibit internally unstable stratification conditions – with an areally distributed buoyancy flux. The ambient velocity field may range from stagnant conditions, to a uniform laminar flow, to a sheared flow, usually with superimposed turbulent fluctuations. In the mean, that velocity field can be steady or time variable, such as under oscillating wave-like or tidal conditions. And the ambient geometry can vary between practically 'unbounded' conditions – in which the spatial scale of the buoyant jet motion is much less than the ambient dimension – as one extreme, to strongly confined conditions as the other. In the latter case, distinctly different phenomena can result, such as jet induced circulations or stratified exchange flows.

In the following attention is restricted to turbulent buoyant jet flows, steady-state in the mean, issuing into an unbounded ambient environment with uniform

density or stable density stratification and under stagnant or steady sheared current conditions. The major area of application for this situation is in the analysis and design of emissions into the environment, both atmosphere and water bodies, for which reliable predictive techniques for purposes of pollution control and mitigation are needed. The assumption of an unbounded environment is a critical one and has to be carefully assessed in each instance as is further stressed below.

While buoyant jets have been a subject of observation and comment throughout the history of science, detailed experimental measurements accompanied by analytical interpretation were commenced by L. Prandtl and disciples in the 1920s. In these works the new framework of boundary layer theory was applied to jet flows as one instance of free turbulent flows that exhibit self-similarity in their gradual evolution along a trajectory. Following measurements on the round [1] and the plane [2] non-buoyant jet, respectively, similarity solutions for the jet evolution (spreading and velocity decay) and for the internal velocity distributions were developed by Tollmien [3], Görtler [4] and Reichardt [5] who used different forms of Prandtl's turbulent mixing length hypothesis for relating the shear stresses to the mean flow. This approach was first extended by Schmidt [6] to the study of the pure vertically rising plume from a round or plane source.

The pioneering work of Reichardt [5, 7] laid the groundwork for the jet integral theory by establishing the Gaussian profile as a satisfactory first-order approximation to jet cross-sectional properties (such as forward velocity or transported scalars) and demonstrating that overall properties of jet behavior can be derived with this a priori assumption. Highly refined measurements whose results formed the basis of much of the ensuing integral jet model development and applications were carried out by H. Rouse and co-workers for the pure jet [8] and the pure plume [9] in both round and plane geometries. They also elucidated the details of the initial zone of flow establishment in which a non-self-similar transition occurs from the efflux condition (more or less top-hat) to the self-similar main region.

Whereas all of the preceding work had viewed jets and plumes as exhibiting 'jet diffusion' whereby fluid momentum, vorticity and scalars are spread by turbulent diffusion, a radically different viewpoint was established in the seminal paper by Morton, Taylor and Turner [10] who applied G.I. Taylor's turbulent entrainment concept to jet and plume flows establishing the 'jet entrainment' hypothesis whereby outside irrotational non-turbulent fluid is entrained, or sucked into, the turbulent jet zone at its edge with a mean velocity that is proportional to the mean centerline velocity. This viewpoint – although the two approaches are quite collorary – offered great advantages in the further adaptation of integral models for buoyant jet configurations of increasing complexities, such as forced plumes in stratified environments [11] and other geophysical flows [12].

The first detailed studies on pure jets discharging into a crossflowing current are due to Jordinson [13] and Keffer and Baines [14] while pure plumes were investigated in the laboratory by Bryant and Cowdrey [15] in addition to the first field observations on smokestack plumes. Scorer [16] and Csanady [17] were the

first to use simple physical reasoning and dimensional arguments to determine the trajectory and growth laws for these cases of source flux/environment interactions as well as associated 'length scales' that delineate regions of influence, such as the transition between weak and strong deflection. The parallel work of Turner [18] and Richards [19] showed that the jet or plume motion in the strongly deflected phase is akin to that in cylindrical line puffs or thermals, i.e., fluid elements that are rising in the ambient due to their initial impulse or buoyancy release. These motions are characterized by an internal double vortex structure that significantly affects velocity and scalar distributions.

The development of reasonably general jet integral models including different source and ambient conditions was started by Abraham [20] still based on the jet diffusion approach and by Fan [21] utilizing the jet entrainment closure. A consistent length scale based categorization of the different buoyant jet regimes in the presence of crossflow and/or stratification was carried out by Wright [22; see also 23]. In subsequent years up to date a large number (several dozens) of buoyant jet models have appeared in the literature. These models, most based on the jet integral formulation, represent many variations on the theme, such as closure assumptions, the use of a Eulerian or a Lagrangian formulation, more or lesser generality of ambient conditions, and the like. No comprehensive review of these diverse modeling efforts is possible here; critical comments, however, pertaining to these models are made in the model formulation that is presented in the following.

In recent years the study of buoyant jets has been greatly enhanced by novel experimental techniques, especially field-based methods such as particle-image velocimetry (PIV) and laser-induced fluorescence (LIF), that provide valuable structural insight into the buoyant jet mixing and entrainment processes as well as more reliable data for model testing and evaluation. Some of these studies will be cited in the model validation section further below.

The purpose of this paper is threefold: First, it sets forth the principles for the integral modeling technique as applied to buoyant jet problems and the minimum conditions that the model formulation must meet and be tested for. Second, it formulates a reasonably rigorous and general jet integral model that has been tested under a wide range of conditions and verified with available high-quality data. Third, it provides limits of applicability for the use of such jet integral models considering the transition to other non-jet like flow processes. The present Part I considers the single buoyant jet issuing from a round orifice, while Part II deals with multiple buoyant jets issuing from multiport diffusers.

2. Fundamental Mechanisms and Integral Modeling Principles

A definition diagram for a buoyant jet in unbounded stratified ambient crossflow is given in Figure 1 in a global Cartesian coordinate system x, y, z in which x points downcurrent and z upward against gravity $\vec{g}$. The ambient has a stable density distributionρ_a (z). ρ_a may given directly, or it may depend on one or more state

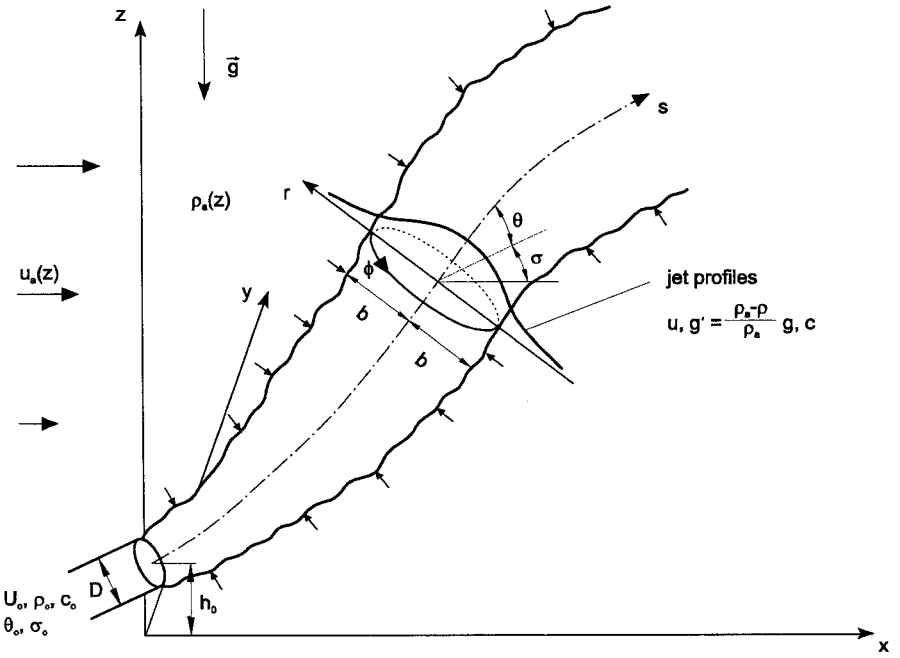

Figure 1. Definition sketch for three-dimensional buoyant jet discharge into ambient flow with global and local coordinate system, respectively.

parameters X_i that are distributed in the vertical, $X_{ia}(z)$, via an equation of state, $\rho = \rho(X_i)$. Typically, X_i would be represented by ambient temperature T_a and salinity S_a for water bodies and by temperature T_a for the atmosphere in which case the potential density concept would be employed, but many other possibilities exist. The ambient also has a sheared velocity profile $u_a(z)$. (Appendix A considers the yet more general case of a skewed velocity profile with an angle $\tau_a(z)$ between the ambient velocity vector at any level and the x axis.)

The jet efflux with diameter D is located at $(0, 0, h_o)$ where h_o is the height above the x-y plane. It is oriented with a vertical angle θ_o above horizontal and a horizontal angle σ_o defined as the angle between the vertical projection of the jet axis and the x axis. The buoyant jet has a nominally unsheared (top-hat) efflux velocity U_o, an efflux density ρ_o – alternatively given by the discharge state parameters, $\rho_o = \rho(X_{io})$ –, and a concentration c_o representing the tracer or pollutant mass of interest. Thus, the buoyant jet is forced by its initial fluxes of momentum M_o and of buoyancy J_o (both in kinematic units)

$$M_o = U_o^2 a_o, \quad J_o = U_o g_o' a_o \tag{1}$$

in which $a_o = D^2\pi/4$ is the discharge cross-sectional area and $g_o' = (\rho_a(h_o) - \rho_o)\, g/\rho_{ref}$ the initial buoyant acceleration where ρ_{ref} is a constant reference density consistent with the Boussinesq approximation. Since M_o is a vector quantity it is useful, alternatively, to define – by means of the discharge angles θ_o and σ_o – the

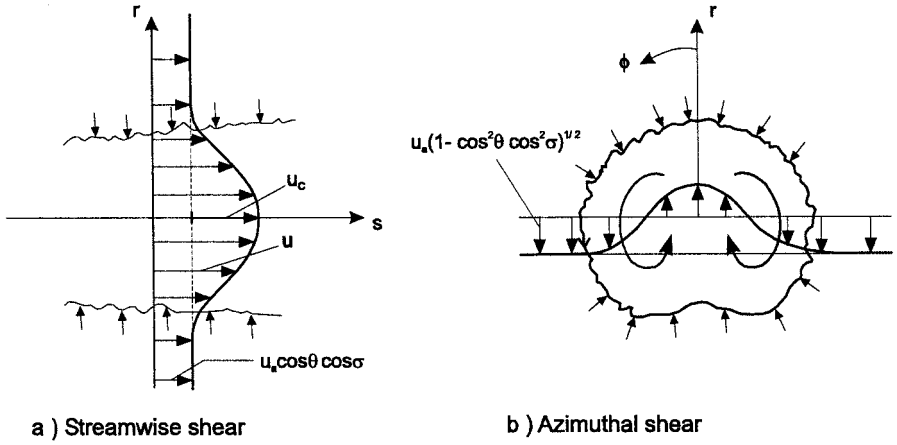

Figure 2. Illustration of the two shear mechanisms leading to entrainment across the laminar-turbulent interface of buoyant jets: (a) Transverse shear due to centerline excess velocity u_c, (b) azimuthal shear due to the transverse propagation velocity $u_a(1-\cos^2\theta_o\cos^2\sigma_o)^{1/2}$.

transverse momentum flux M_{ot} and the excess longitudinal momentum flux M_{oe}

$$M_{ot} = M_o(1 - cos^2\theta_o cos^2\sigma_o)^{1/2}, \quad M_{oe} = Q_o\,(U_o\cos\theta_o\cos\sigma_o - u_a) \qquad (2)$$

for the momentum forcings away from and along the x-direction, respectively. The initial mass flux

$$Q_{co} = U_o c_o a_o \qquad (3)$$

is a passive quantity without dynamic influence. The initial discharge (volume flux) $Q_o = U_o a_o$ used in Equation (2) is a quantity that has limited dynamic influence in the discharge vicinity only, in the so-called zone of flow establishment (ZOFE).

Figure 1 sketches the spatial evolution of the buoyant jet along a trajectory s. Relative to the outside laminar (or weakly turbulent) flow, several free turbulence shearing mechanisms lead to strong turbulent fluctuations within the jet and a gradual growth of its characteristic width b. The primary condition for a fully turbulent jet flow is a sufficiently high value of the exit Reynolds number

$$Re_o = U_o D/\nu \qquad (4)$$

in which $\nu$is the kinematic viscosity. Under these conditions the jet behavior, notably its dominating large-scale fluctuation, mixing and entrainment aspects, becomes independent of viscosity. For a simple jet into a stagnant ambient a generally accepted critical value for Re_o is about 2000 [23]. When more forcing factors, such as buoyancy or crossflow, come into play the critical value is yet lower (e.g., about 1000 for the pure plume; Ungate, 1974).

A local cylindrical coordinate system (Figure 1) with axial distance s, radial distance r and azimuthal angle ϕ is defined along the trajectory, and inclined

with the local horizontal angle θ and horizontal angle σ. Two types of shearing mechanisms (see Figure 2) can be distinguished in this coordinate system: (1) Streamwise shear τ_{rz} in which the velocity excess above the ambient component $u_a \cos\theta_o \cos\sigma_o$ causes primary instabilities in form of axisymmetric ring vortices that with superimposed secondary instabilities ultimately break down into three-dimensional turbulence. Mean entrainment occurs uniformly at the jet periphery. (2) Azimuthal shear $\tau_{r\phi}$ in which the ambient flow with normal component $u_a(1 - \cos^2\theta_o \cos^2\sigma_o)^{1/2}$ passes around, and interacts with, the cylindrical jet element. The shear at the element flanks leads to instabilities, causes cumulative entrainment predominantly in the lee and sets up an internal double vortex circulation.

The objective of any jet analysis is the determination of the jet trajectory $x(s)$, $y(s)$, $z(s)$, the geometrical factors $\theta\,(s)$, $\sigma\,(s)$, along with the distributions $f(r, \phi)$ for the local axial velocity u, density ρ (or alternatively, state parametersX_i) and concentration c. In the case of the jet integral method, the distribution functions $f(r, \phi)$ are specified *a priori* and cease to be object of analysis. This approach is obviously inspired by the tenets of self-similarity for simple free turbulence motions (e.g., jets, wakes), but can only be approximate for the general buoyant jet that is not in equilibrium, but rather in transition among five possible states of self-similarity, as is shown below. With this restriction the following distribution functions

$$\begin{aligned} u &= u_c e^{-r^2/b^2} + u_a \cos\sigma \cos\theta, \quad g' = g'_c e^{-r^2/(\lambda b)^2}, \\ \mathrm{X}_i &= \mathrm{X}_{ic} e^{-r^2/(\lambda b)^2} + \mathrm{X}_{ia}\,(z)\,, \quad c = c_c e^{-r^2/(\lambda b)^2} \end{aligned} \tag{5}$$

based on Gaussian profiles are the most reasonable, in which $u_c$is the excess axial velocity, $g'_c = (\rho_a\,(z) - \rho_c)\,g/\rho_{ref}$ the buoyancy, ρ_c the density, X_{ic} the excess value of the state parameters, and $c_c$the concentration, all on the centerline. b is a measure of the jet width where the excess velocity is $e^{-1} = 37\%$ of the centerline value, $\lambda > 1$is a dispersion ratio as the observed width of the scalar distribution is larger than for the velocity (turbulent Schmidt number). These fully axisymmetric profiles, functions$f\,(r)$ only, are an excellent representation to all free turbulent flows with streamwise shear as evidenced by numerous comparisons with experimental data for jets, plumes or wakes. They are obviously less satisfactory for the double peaked distributions of axial velocity and scalars in the crossflow dominated buoyant jet phases that show an internal vortex pair (Figure 2b), but still serve as a useful first approximation.

The jet integral method proceeds by making use of the boundary-layer nature of the flow and by integrating all terms ( ) of the governing turbulent Reynolds equations of motion (not stated herein) across the cross-sectional plane, $\int (\,)\,dA$ in which $dA = r\,d\phi\,dr$. A system of ordinary differential equations is the result and major advantage of this procedure. For the given axisymmetric profiles the integration amounts to $2\pi \int_0^{R_j} (\,)\;dr$. The 'jet radius' R_j is understood in boundary-layer parlance as the 'edge of the jet' at which boundary conditions can

be clearly specified or, alternatively, beyond which no further contributions to the integration should arise. This is a crucial point in some of the integrals as will be explained below. Also, a number of 'turbulence closure coefficients' arise in the course of the integration process.

The following principles must be met for a reasonably accurate application of the jet integral method:

Principle 1: The integral method is strictly valid only for the five asymptotic conditions in which a fully self-similar flow with a constant internal force balance and invariant turbulence properties are maintained.

In an environment with constant velocity u_a and a constant gradient of buoyancy $\varepsilon = -(g/\rho_a)(d\rho_a/dz)$ and beyond the initial ZOFE, the buoyant jet behavior is controlled by the interplay of the parameters u_a, ε, J_o, M_o, θ_o, σ_o (or M_{ot} and M_{oe}, Equation (2), in place for the latter three). Five regimes with self-similar turbulent flow characteristics can be defined as special cases of these forcing functions:
(i) Pure jet: $u_a = 0$, $\varepsilon = 0$, $J_o = 0$; source of M_o only. The jet proceeds in the direction prescribed by θ_o and σ_o.
(ii) Pure plume: $u_a = 0$, $\varepsilon = 0$, $\sigma_o = 90°$; source of J_o only. The plume rises vertically.
(iii) Pure wake: $\varepsilon = 0$, $J_o = 0$, $\theta_o = 0$, $\sigma_o = 0$, $M_{ot} = 0$; source of M_{oe} only (whereby $M_{oe} \ll M_o$; i.e. a weak momentum excess only) in u_a. The wake motion develops in the ambient flow.
(iv) Advected line puff: $\varepsilon = 0$, $J_o = 0$, $M_{oe} = 0$; source of M_{ot} only. The transverse momentum injected into the flow sets up a cylindrical line puff that propagates transversely into the flow while being advected.
(v) Advected line thermal: $\varepsilon = 0$, $M_{oe} = 0$, $M_{ot} = 0$ (i.e., $\sigma_o = 0$, $\theta_o = 0$); source of J_o only in u_a. The buoyancy flux causes a vertically rising cylindrical thermal while being advected.

Of these regimes, the first three are dominated by streamwise shear and the last two by azimuthal shear. In actual discharge situations one or more of the five regimes can occur as asymptotic regimes. The jet regime (i) is often the initial regime (whenever $U_o \gg u_a$) and the advected thermal regime (v) is usually – but not always – the concluding regime.

Exact theoretical formulations and a good experimental data base that allows the specification of the closure coefficients exist for these five regimes. Thus, any general jet model formulation must – as a minimum test – be shown to be consistent with these regimes!

Principle 2: The formulation of the transitions between these regimes, e.g., the variability of coefficient values, is arbitrary. Transition functions cannot be derived from first principles. Their formulation should primarily be guided by pragmatism and a good overall data fit when testing the model under general transition conditions. Fortunately, jet integral models behave quite acceptably in this regard provided all the other principles are maintained.

Principle 3: Jet integral models cannot be expected to hold for flow situations in which boundary layer behavior is no longer maintained. The boundary layer approximation implies a pressure within the jet equal to that in the outside ambient. This is violated whenever the jet undergoes strong spreading or exhibits strong curvature. Examples for the first are the terminal layer transition in ambient stratification, for the second jets into an opposing ambient current. In this context, note also that none of the self-similar asymptotic regimes outlined above include ambient density stratification, $\varepsilon \neq 0$. In that case, axial pressure forces influence and finally destroy the boundary-layer evolution of the flow and lead to strong horizontal spreading, the so-called collapse motion during the terminal layer phase of a buoyant jet in stratified surroundings. The flow is no longer jet-like. This makes futile past attempts to extend jet model predictions into the terminal layer phase.

Principle 4: The initial zone of flow establishment (ZOFE) is another transition region that lacks self-similarity as the initial unsheared profiles undergo changes in form of peripherally growing axisymmetric mixing layers until the final jet profiles are reached. This transition is quite complex, in particular for ambient crossflow, on one hand, and reasonably rapid, up to a distance of about (5 to 10)D, on the other. Give the overall jet region of interest an empirical formulation based on experimental observations is therefore most appropriate for the ZOFE.

Principle 5: The jet integral equations should be formulated in terms of flux quantities rather than local variables (such as b, u_c, etc.). The flux quantities are mostly conservative (i.e., strictly constant or gradually changing) while local variables can undergo strong changes or contain singularities (e.g., at the point of maximum rise for a vertical negatively buoyant jet in stagnant ambient) which affects solution accuracy. This principle cannot be always maintained as is shown below but should be aimed for.

Principle 6: All jet integral model formulations must be accompanied by limits of applicability in form of spatial restrictions. When carried beyond these limits the models predict unrealistic or nonsensical behavior. For example, the turbulent entrainment for a jet in crossflow will at some distance be dominated by turbulent mixing in the existing ambient flow, or models applied to buoyant jets in stratified crossflows predict a final stage with persistent oscillations around the terminal level which are unrealistic as the jet is laterally collapsing in that stage. This issue becomes critical when integral models are applied to finite receiving domains in which jet boundary interactions either terminate or significantly alter the jet motion.

3. Integral Model Formulation

3.1. MODELING STRATEGY

Irrespective of their formulation integral models are approximate. A series of choices need to made in the formulation. These should be dictated by convenience and simplicity but should satisfy the principles set forth in the preceding section.

First, since the flow field is steady in the mean a Eulerian formulation for the evolution along the trajectory is straightforward and preferable. In contrast, a number of integral models have been written in a Lagrangian framework in which a jet element is assumed to be advected with a some average local velocity along the trajectory [24, 25]. During that advection the element is assumed to be transformed through various entrainment and force mechanisms. This approach is quite appealing for the limiting final stages of strong advection, but in the initial jet stages it seems awkward in comparison to a simple Eulerian formulation.

Secondly, the governing equations of motion and turbulent transport (Reynolds equations) need to be integrated in the local coordinate system using the profile specifications, Equation (5). This yields a system of conservation equations for different flux quantities. A simpler alternative that will be pursued herein is to first define such flux quantities in a fashion that describes the total transport of volume, momentum and scalar mass in the turbulent jet zone and then state conservation principles for these quantities. Even though the latter alternative can be shown [26] to contain some inaccuracies because of the reversal of integration and differentiation (for which Leibnitz's rule needs to be applied) it appeals as a simple and direct approach. The inaccuracies are minor relative to other modeling assumptions and irrelevant if the full model formulation satisfies the five asymptotic regimes.

Thirdly, the gradual growth of the turbulent zone can be described through a spreading equation [27] or through an entrainment model. In the asymptotic cases, both approaches can be shown to be linked. In the general case, however, an entrainment model appeals physically due to its direct linkage between turbulent growth and forcing functions, i.e., the diverse shear mechanisms.

The following model formulation expands on the approach first taken by Jirka and Fong [28].

3.2. INTEGRAL QUANTITIES

Through cross-sectional integration the following bulk variables for total volume flux Q, axial momentum flux M, buoyancy flux J, flux of excess state parameter $Q_{\mathrm{X}i}$ and tracer mass flux Q_c, respectively, are obtained

$$Q = 2\pi \int_0^{R_j} urdr = \pi b^2 \left(u_c + 2u_a \cos\theta \cos\sigma\right), \tag{6}$$

$$M = 2\pi \int_0^{R_j} u^2 rdr = \frac{1}{2}\pi b^2 \left(u_c + 2u_a \cos\theta \cos\sigma\right)^2, \tag{7}$$

$$J = 2\pi \int_0^{R_j} ug'rdr = \pi b^2 \left(u_c \frac{\lambda^2}{1+\lambda^2} + \lambda^2 u_a \cos\theta \cos\sigma\right) g'_c, \tag{8}$$

$$Q_{\mathrm{X}i} = 2\pi \int_0^{R_j} u\left(\mathrm{X}_i - \mathrm{X}_{ia}\right) rdr = \pi b^2 \left(u_c \frac{\lambda^2}{1+\lambda^2} + \lambda^2 u_a \cos\theta \cos\sigma\right) \mathrm{X}_{ic}, \tag{9}$$

$$Q_c = 2\pi \int_0^{R_j} ucrdr = \pi b^2 \left(u_c \frac{\lambda^2}{1+\lambda^2} + \lambda^2 u_a \cos\theta \cos\sigma \right) c_c. \tag{10}$$

When evaluating the individual terms in these flux quantities the integration limit R_j is usually taken as $R_j \to \infty$ as the definite integrals over the jet profiles, Equation (5), yield bounded values. There are two exceptions in the crossflow contributions (second terms under the parenthesis) for Q and M, respectively, in which $R_j = \sqrt{2}b$. Recent detailed measurements by Chu [29] using the LIF method for a co-flowing jet support this choice of the jet radius with the purpose of defining the turbulent jet flow region in which the actual transport and mixing process occurs. On the basis of Equation (5), $R_j = \sqrt{2}b$ defines a local velocity excess of 14% and scalar value of 25% (with a typical $\lambda = 1.20$) of the centerline values. The latter value describes the location of the instantaneous laminar/turbulent interface of the jet as is shown in Figure 3 by virtue of the intermittency distribution, the distribution of maximum and minimum concentration profiles, and a comparison of an instantaneous cross-section and the $0.25c_c$ value of the average cross-section. Incidentally, this definition of R_j agrees with a long tradition in the visual analysis of atmospheric plumes and happens to be consistent in a flux sense with the much cruder top-hat profile assumption [30].

3.3. CONSERVATION EQUATIONS

Conservation equations for the flux quantities defined by Equations (6) to (10) are formulated for a jet element of length ds centered on the trajectory. The following assumptions are made: (1) Pressure deviations from hydrostatic within the jet are neglected consistent with the boundary layer nature of the flow; (2) acceleration effects due to jet curvature are neglected; (3) turbulent momentum and scalar fluxes are neglected relative to the mean fluxes of momentum and scalars. Typically these terms amount to some 10% of the mean values [31, 32], but more importantly they are proportional to the mean values so there is no need for a separate representation.

The conservation principles for volume (continuity), momentum components in the global directions x, y and z, state parameters, and scalar mass lead to the following equations

$$\frac{dQ}{ds} = E, \tag{11}$$

$$\frac{d}{ds}(M \cos\theta \cos\sigma) = E u_a + F_D \sqrt{1 - \cos^2\theta \cos^2\sigma}, \tag{12}$$

$$\frac{d}{ds}(M \cos\theta \sin\sigma) = -F_D \frac{\cos^2\theta \sin\sigma \cos\sigma}{\sqrt{1 - \cos^2\theta \cos^2\sigma}}, \tag{13}$$

$$\frac{d}{ds}(M \sin\theta) = \pi \lambda^2 b^2 g_c' - F_D \frac{\sin\theta \cos\theta \cos\sigma}{\sqrt{1 - \cos^2\theta \cos^2\sigma}}, \tag{14}$$

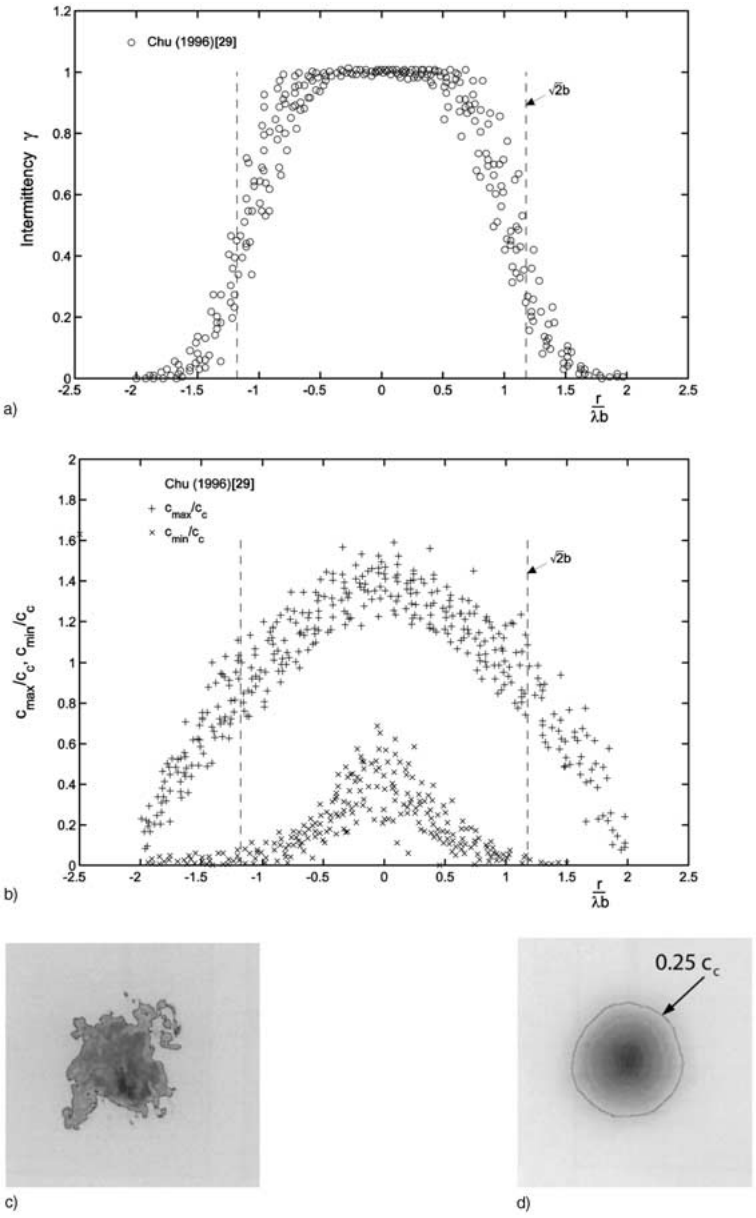

Figure 3. Definition of jet radius $R_j = \sqrt{2}b$ as the integration limit for the flux quantities in the advected buoyant jet stages marking the width of the turbulent transport zone. Data by Chu [29] for the co-flowing jet. (a) Concentration intermittency γ, (b) maximum/minimum concentration values, $c_{\max}/c_c$, $c_{\min}/c_c$, both as function of radial distance, $r/(\lambda b)$, where $\lambda = 1.20$, (c) LIF images of instantaneous and (d) averaged concentration values in a jet cross-section.

$$\frac{dQ_{Xi}}{ds} = -Q\frac{dX_{ia}}{dz}\sin\theta, \tag{15}$$

$$\frac{dQ_c}{ds} = 0. \tag{16}$$

Furthermore, the geometry of the trajectory is defined by

$$\frac{dx}{ds} = \cos\theta\cos\sigma, \quad \frac{dy}{ds} = \cos\theta\sin\sigma, \quad \frac{dz}{ds} = \sin\theta \tag{17}$$

and the centerline density ρ_c contained in the definition of centerline buoyancy g_c' in Equation (14) is given by the equation of state

$$\rho_c = \rho_c\left(\mathrm{X}_{ic}\right). \tag{18}$$

Appendix A lists two specific examples for equation of states in temperature- and salinity-stratified water bodies and the stratified atmosphere, respectively. Whenever a simple linearized equation of state applies then an equation for the conservation of buoyancy can be used in lieu of Equations (15) and (18)

$$\frac{dJ}{ds} = Q\frac{g}{\rho_{ref}}\frac{d\rho_a}{dz}\sin\theta. \tag{19}$$

The terms E and F_D in the equations above represent the entrainment rate and an ambient drag force acting on the jet element. The specification of these turbulent processes constitutes the 'turbulence closure problem' in the integral formulation. The force term Eu_a in Equation (12) is the entrainment of ambient momentum into the jet and the term $\pi\lambda^2 b^2 g_c'$ in Equation (14) the buoyancy force. The right hand terms in Equations (15) and (19), respectively, represent the dilution effect as the jet moves through the stratified environment.

The entrainment rate E is specified as the additive contributions of the different streamwise and azimuthal shear mechanisms that lead to entrainment of ambient fluid into the turbulent jet proper

$$\begin{aligned} E \;=\; & 2\pi b u_c\left(\alpha_1 + \alpha_2\frac{\sin\theta}{F_\ell^2} + \alpha_3\frac{u_a\cos\theta\cos\sigma}{u_c+u_a}\right) + \\ & + 2\pi b u_a\sqrt{1-\cos^2\theta\cos^2\sigma}\;\alpha_4\left|\cos\theta\cos\sigma\right|. \end{aligned} \tag{20}$$

Following a long-standing convention the entrainment velocity is prescribed at a distance equal to the e^{-1} width b (rather than the radius $R_j = \sqrt{2}b$ that would be more appropriate for the entrainment process) and this arbitrary choice is reflected in the numerical value of the entrainment coefficients α_1 to α_4. The streamwise entrainment terms are proportional to the centerline velocity u_c and are given by coefficient values for the pure jet α_1, and the added effect of the pure plume α_2 and the pure wake α_3, respectively. The pure plume contribution is inversely proportional to the square of the local densimetric Froude number $F_\ell = u_c/\sqrt{g_c' b}$

and depends on the vertical angle θ. Such a functional transition can be derived by means of a mean kinetic energy equation as first suggested by Fox [33]. The pure wake enhancement is proportional to the wake parameter $u_a/(u_c + u_a)$. The azimuthal entrainment scales with the ambient velocity component transverse to the jet $u_a\sqrt{1 - \cos^2\theta\cos^2\sigma}$ and the coefficient α_4 represents both line puff and thermal. In the latter two terms, the projection term $|\cos\theta\cos\sigma|$ accounts for the deviation of the jet element axis from the direction of the crossflow.

The jet drag F_D is parameterized as a quadratic law force mechanism

$$F_D = c_D 2\sqrt{2}b\frac{u_a^2(1 - \cos^2\theta\cos^2\sigma)}{2}, \tag{21}$$

in which $u_a\sqrt{1 - \cos^2\theta\cos^2\sigma}$ is the transverse velocity component, $2\sqrt{2}b$ the jet diameter, and c_D the drag coefficient. Equation (21) specifies a drag effect in obvious analogy to the flow around a cylindrical solid body for which boundary layer separation leads to a pressure reduction in the lee of the body and a turbulent wake that is distinguished by a momentum deficit flux and a vorticity field consisting of unsteady counterrotating vortices.

Since an entraining jet is quite dissimilar in character there has been much controversy in the literature as to the existence and precise nature of a turbulent jet drag force F_D and whether it is of any importance in Equation (21) relative to the entrainment of ambient momentum Eu_a (often called the entrainment force). Fric and Roshko [34] have shown that up to four vortex types may exist for a jet in a crossflow, in particular when it is issuing out of a bounding wall. Of major interest for the present argument is here the existence of a wake vortex structure downstream of the jet. Fric and Roshko have clearly demonstrated these wake vortices for the case of strong crossflow with a jet that is issuing flush from the bounding wall. They attribute its existence partly to an interaction with the wall boundary layer. However, other studies have shown that the wake vortices exist also for very weak crossflows and far from the wall [35] and for jets issuing from an elevated source [36–38]. The study by Moussa *et al.* [36] in particular, clearly demonstrates the vortex-shedding system in the wake of the jet for well elevated effluxes. Eiff and Keffer [37] show that a lock-in between the elevated stack wake and the jet wake occurs over a wide parameter range. Detailed pressure measurements for the situation in which the jet issues from a bounding wall show that a drag coefficient evaluated from the pressure distribution at the jet periphery and at the bounding wall (efflux plane) varies between about 0.8 for weak to about 3.0 for strong crossflows [39]. These coefficients seem to include, however, the contributions due to the pressure due to the pressure field of the entraining sink flow. Additional pressure measurements are summarized by Margason [40]. Measurements in a line directly downstream of the jet by Fric and Roshko [34] give further support of a reduced pressure zone. The data of Smith and Mungal [35] as well as those of Davidson and Pun [38] show in addition that some jet fluid is actually carried into the trailing vortex zone. All these evidences point to the fact that beyond the mere

entrainment force there is another jet/crossflow interaction mechanism that can in first order be parameterized as a quadratic law drag force. Clearly, more work needs to be done to further elucidate the precise mechanism and the order of magnitude of this effect. The extreme assertion of Morton and Ibbetson [41] that a turbulent wake with rotational effects and vortex lines parallel to the z-axis simply cannot exist because such vorticity is not generated due to absence of a solid boundary is clearly not upheld by the experimental evidence. Furthermore, that assertion seems invalid in any case as the vortex stretching effect due to the velocity field imposed by the jet inflow leads to a re-orientation of the initial vorticity that lies embedded in the ring-like shear-layer vortices at the influx jet periphery: Of course, there cannot be any net vorticity with a z-component, but there can be individual vortex elements, in particular turbulent fluctuations, in the wake zone as observed in the above mentioned studies. This view is further corroborated by the detailed vortex visualization studies of Kelso *et al.* [42] and the large-eddy simulations of Yuan *et al.* [43].

3.4. INITIAL CONDITIONS: ZONE OF FLOW ESTABLISHMENT (ZOFE)

The nine governing equations for flux conservation and jet geometry, Equations (11) to (17), – together with the supplemental equations of state, Equation (18), for entrainment, Equation (20), and the drag force, Equation (21) – describe the evolution of the nine jet variables, Q, M, $Q_{\mathrm{X}i}$(alternatively J), Q_c, θ, σ, x, y and z. The numerical solution of the equation system is carried out with a fourth-order Runge–Kutta algorithm. The formulation given above uses essentially a flux-conservative formulation (following Principle 5) that minimizes the effect of potential singularities. The use of some of the local variables, b, u_c, g_c' and X_{ic}, cannot be avoided altogether. Supplemental relationships for these variables can be derived from the flux definitions. These are summarized in Appendix B.

Initial conditions need to be specified at the jet efflux. As noted in Section 2, the actual jet discharge conditions occur at some location $(0, 0, h_o)$ where nominally unsheared efflux conditions occur, or in practice, the jet exit velocity profile may contain peripheral boundary layers characteristic of a nozzle flow or of a longer preceding pipe flow section. These conditions are described by the initial values of the flux variables, M_o, J_o (see Equation (1)) and Q_{co} (Equation (3)) and the initial angles θ_o and σ_o. Two non-dimensional measures, a crossflow parameter R and a densimetric Froude number F_o

$$R = \frac{U_o}{u_a}, \quad F_o = \frac{U_o}{\sqrt{g_o' D}} \tag{22}$$

characterize the crossflow and buoyancy interaction of the discharge, respectively.

The transition from that more or less uniform efflux section to a fully established jet flow that can be characterized by the approximately self-similar distribution functions given by Equation (5) takes place in the ZOFE. There have been many

attempts to construct detailed models of the ZOFE mechanics with the developing shear layer at the jet periphery. However, all these are limited to special conditions, e.g. for the pure jet in stagnant ambient by Abramovich [44], or for the vertically rising pure plume by Lee and Jirka [45]. The transition process for general conditions of crossflows under arbitrary discharge angles and with discharge buoyancy is highly complex. Thus, a detailed treatment seems both futile and unnecessary (see Principle 4) in view of the limited extent of the ZOFE.

The following approximate model of the ZOFE proceeds from the case of a pure jet in stagnant ambient for which momentum conservation, $M_e = M_o$, shows that $Q_e = \sqrt{2}\, Q_o$ by virtue of Equations (6) and (7). Subscript e denotes conditions at the end of the ZOFE. The ZOFE length L_e is found from a linear spread of the shear layer to be about 6.2 D based on velocity profiles or about 5.0 D based on scalar profiles, due to the typical dispersion ratio, $\lambda > 1$. This basic result is extended to general conditions using the empirical approach of Schatzmann [26] for crossflow effects and the model formulation of Lee and Jirka [45] for buoyancy effects. Supplementary discharge angles are defined as

$$\gamma_o = \sin^{-1}(\sqrt{1 - \cos^2\theta_o \sin^2\sigma_o}, \quad \delta_o = \tan^{-1}(\tan\theta_o / \sin\sigma_o) \tag{23}$$

in which γ_o is the transverse discharge angle relative to the ambient current direction and δ_o its projection onto the x-y plane. The modified ZOFE length L_e and its final transverse angle γ_e are

$$L_e = 5.0D\,(1 - 3.22\,\sin\gamma_o/R)\,(1 - e^{-2.0F_o/F_{\ell p}}), \tag{24}$$

$$\gamma_e = \tan^{-1}\left(\frac{\sin\gamma_o}{\cos\gamma_o - (\sqrt{2}-1)/R}\right), \tag{25}$$

in which $F_{\ell p}$ is the asymptotic value of the local densimetric Froude number (defined in Equation (20)) of a pure plume (see next section). Hence the initial conditions for the solution of the jet equation system can be stated, for the geometry

$$\theta_e = \sin^{-1}(\sin\gamma_e \sin\delta_o), \quad \sigma_e = \tan^{-1}(\sin\gamma_e \cos\delta_o / \cos\gamma_e), \tag{26}$$

$$x_e = L_e \cos\theta_{ave} \cos\sigma_{ave}, \quad y_e = L_e \cos\theta_{ave} \sin\sigma_{ave}, \quad z_e = h_o + L_e \sin\sigma_{ave} \tag{27}$$

in which $\theta_{ave} = (\theta_o + \theta_e)/2$ and $\sigma_{ave} = (\sigma_o + \sigma_e)/2$, and for the fluxes

$$Q_e = \sqrt{2}\, Q_o, \quad M_e = M_o, \quad Q_{\mathrm{X}ie} = Q_{\mathrm{X}io}\ (or\ J_e = J_o), \quad Q_{ce} = Q_{co}, \tag{28}$$

respectively.

4. Model Evaluation and Data Comparison

The equation system and solution procedure outlined in the preceding Section has been coded with input and graphical output routines into the Fortran program CorJet. The following coefficients are used in CorJet:

$$\begin{array}{llll} \alpha_1 = 0.055, & \alpha_2 = 0.6, & \alpha_3 = 0.055, & \alpha_4 = 0.5 \\ \lambda = 1.20, & c_D = 1.3\,. & & \end{array} \tag{29}$$

In essence, these parameters constitute 'turbulence closure' coefficients for the complex turbulent mixing process. Six values are needed to guarantee precise predictions for all of the asymptotic self-similar regimes with their different mixing dynamics. The choice of these parameter values will be commented upon further below.

Different scalings will be used to display model predictions and to compare to experimental data. In some instances, lengths will be scaled by the diameter D and dynamic conditions indicated by the parameters, R and F_o, Equation (22). In most cases, however, dynamic length scales are the preferred choice for displaying buoyant jet characteristics [22, 46]:

$$\begin{array}{lll} \text{Jet/plume transition length scale} & L_M = M_o^{3/4}/J_o^{1/2} \\ \text{Jet/crossflow length scale} & L_m = M_o^{1/2}/u_a \\ \text{Plume/crossflow length scale} & L_b = J_o/u_a^3 \\ \text{Jet/stratification length scale} & L'_m = M_o^{1/4}/\varepsilon^{1/4} \\ \text{Plume/stratification length scale} & L'_b = J_o^{1/4}/\varepsilon^{3/8}. \end{array} \tag{30}$$

The jet mixing characteristics are measured by two dilution values, the centerline dilution $S_c = c_o/c_c$ (referring to a conservative substance) and the bulk dilution $\bar{S} = Q/Q_o$, respectively. By virtue of the definitions, Equations (6) and (10), and since $Q_c = Q_{co}$, these dilutions are related as

$$\frac{\bar{S}}{S_c} = \frac{u_c + 2\,u_a \cos\theta \cos\sigma}{u_c\,\lambda^2/(1+\lambda^2) + \lambda^2 u_a \cos\theta \cos\sigma}. \tag{31}$$

Hence, for strong jet- or plume-like flows, $u_c \gg u_a$, $\bar{S} \cong 1.7\,S_c$, while for strongly advected flows $u_a \gg u_c$, $\bar{S} \cong 1.4\,S_c$. These expected ratios are consistent with the detailed measurements of Chu *et al.* [47].

4.1. THE FIVE ASYMPTOTIC REGIMES

For the cases of the pure jet, plume and wake, respectively, all with the controlling transverse shear mechanism, the entrainment velocity u_e at the nominal jet width b is proportional to the centerline velocity, $u_e \sim u_c$.

The **pure jet** is parameterized by an entrainment coefficient $\alpha_{jet} = \alpha_1 = 0.055$ for the Gaussian jet profile so that $u_e = \alpha_{jet} u_c$. This value, as well as the dispersion

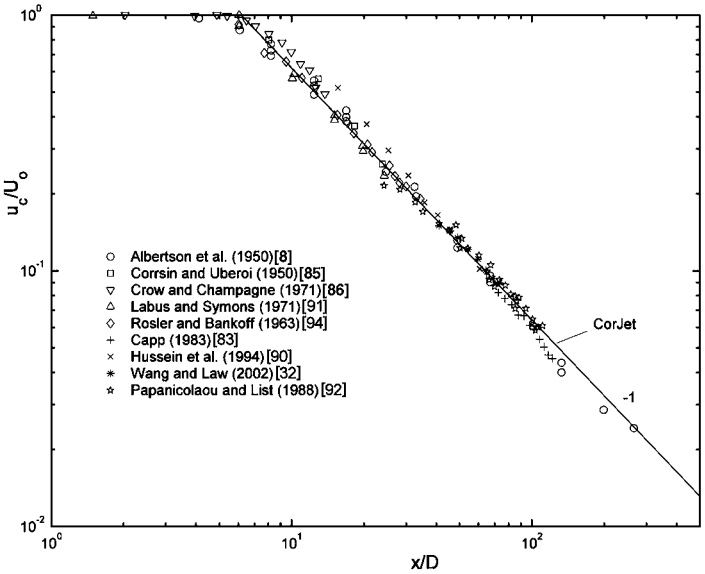

Figure 4. Pure jet: Comparison of experimental data for the decay of centerline velocity u_c/U_o as function of axial distancex/D with integral model predictions.

ratio $\lambda = 1.20$ are derived from the extensive data surveys of Chen and Rodi [48] and List [31], but also agree with more recent work using PIV and LIF techniques [32]. Differences in observed values between various experimenters are typically $\pm 5\%$. Figure 4 shows the decay of centerline velocity u_c/U_o and Figure 5 the bulk dilution $\bar{S}$, both as a function of axial distance x/D, with data from different experimental sources. The CorJet model does not resolve the details within the ZOFE, but captures the behavior in the self-similar zone.

The internal force balance in the **pure plume** motion is characterized by the asymptotic value $F_{\ell p}$ of the densimetric Froude number $F_\ell = u_c/\sqrt{g'_c b}$. This sets the plume coefficient $\alpha_{plume} = 0.055 + 0.6/F_{\ell p}^2$ for the entrainment velocity $u_e = \alpha_{plume}\, u_c$. The value $F_{\ell p}$ can be found from the condition $\frac{dF_\ell^2}{ds} = 0$ that derives from the conservation equations for volume, vertical momentum and buoyancy flux, Equations (11), (14) and (19), respectively. This approach (see [49]) leads to

$$F_{\ell p}^2 = \frac{5}{4}\frac{\lambda^2}{\alpha_{plume}}. \tag{32}$$

Inserting the definition for α_{plume} into this equation yields the asymptotic values $\alpha_{plume} = 0.083$ and $F_{\ell p} = 4.67$. Again, these values are in general agreement with the available data sources. The dispersion value of $\lambda = 1.20$ for the pure jet is also adequate for the pure plume [31], even though more recent studies appear to suggest an about 10% lower value [32, 92].

Available experimental studies are never limited to the pure plume regime, but for experimental reasons usually include the transition from a more jet-like initial

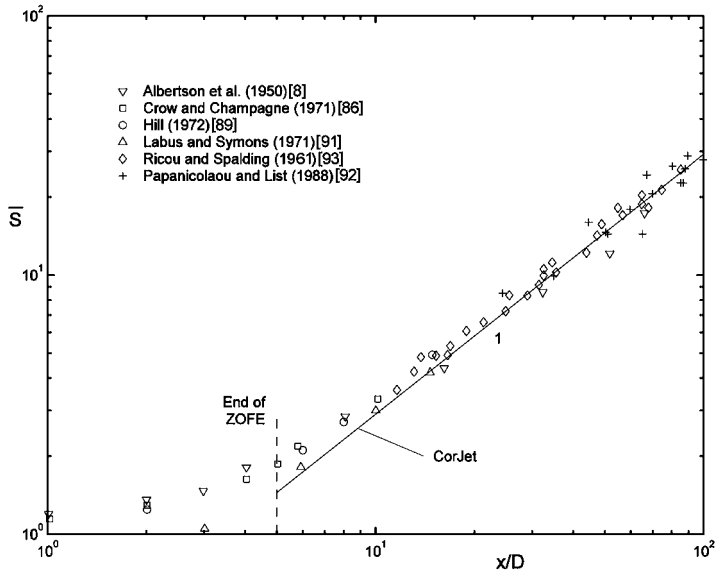

Figure 5. Pure jet: Bulk dilution $\bar{S}$ as function of axial distance x/D.

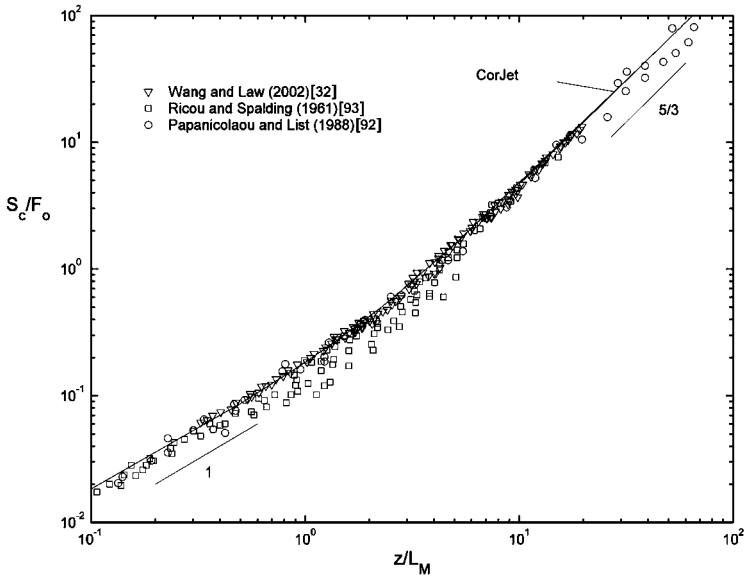

Figure 6. Vertical buoyant jet in stagnant ambient: Normalized centerline dilution S_c/F_o as a function of vertical distance z/L_M. The slopes indicate the asymptotic stages, $S_c \sim z^1$ for the jet and $S_c \sim z^{5/3}$ for the plume.

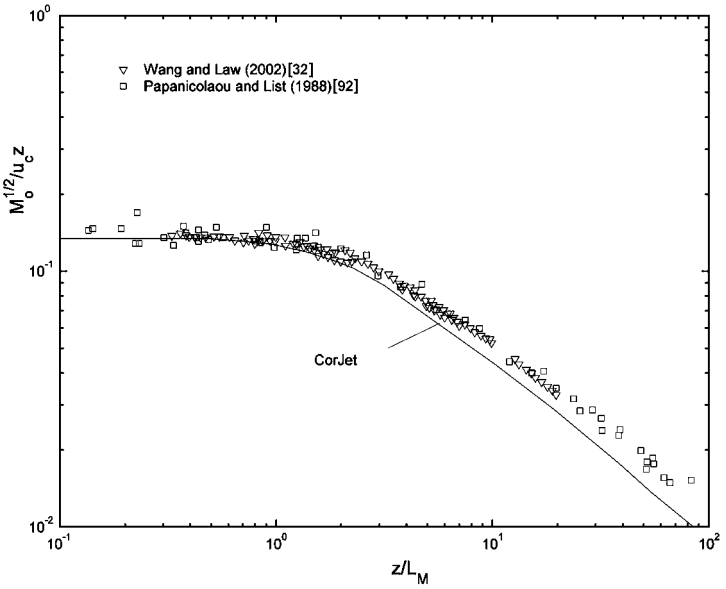

Figure 7. Vertical buoyant jet transition in stagnant ambient: Normalized inverse centerline velocity $M_o^{1/2}/(u_c\, z)$ as a function of vertical distance z/L_M. The slopes are $u_c \sim z^{-1}$ for the jet and $u_c \sim z^{-1/3}$ for the plume.

regime to the final plume motion. Figure 6 shows the normalized centerline dilution S_c/F_o as a function of vertical distance z/L_M. The transition from a dependence $S_c \sim z^1$ for the jet to for the plume is evident. The transition region is given by the range $1 < z/L_M < 5$ [92]. The CorJet predictions agree well with the experimental data by various investigators that represent for one part direct measurements of centerline concentrations c_c and for the other part conversions via Equation (31) from volume flux measurements Q. Figure 7 gives the comparison for the normalized centerline velocity inverse $M_o^{1/2}/(u_c\, z)$ as a function of z/L_M. Again, the transition from the jet $u_c \sim z^{-1}$ to the plume $u_c \sim z^{-1/3}$ is evident. The CorJet predictions for the plume regime agree in trend, but the predicted u_c values lie some 30% above the two experimental sources, which is surprising since the bulk volume flux (see Figure 6) agrees well. This may be related to strong initial source effects (low F_o) that appear to dominate the experimental range with high z/L_M in which the flow may be away from similarity as remarked by Wang and Law [32].

For the co-flowing **pure wake** (with $u_c \ll u_a$, $\theta = 0°$ and $\sigma = 0°$) the entrainment coefficient in Equation (20) becomes $\alpha_{wake} = \alpha_1 + \alpha_3 = 0.110$ so that the wake entrainment velocity $u_e = \alpha_{wake}\, u_c$ is twice as large as for the jet. The pure wake has the following evolutionary laws $b \sim x^{1/3}$ and $u_c \sim x^{-2/3}$ that can be obtained from the governing equations, Equation (11) and (12). Due to experimental limitations it is quite difficult to observe the pure wake regime of a jet efflux. Also high quality experimental data on the jet/wake transition have not been available until the recent study of Nickels and Perry [50] in which special precau-

tions were taken to eliminate the negative wake effect of the discharge nozzle. Figure 8a shows their data for the decay of the normalized centerline velocity u_c/u_a as a function of downstream distance x/L_{me} in which $L_{me} = M_{oe}^{1/2}/u_a$ is the modified jet/crossflow length scale based on the excess momentum flux M_{oe} (see Equation (2)). The growth of the width b/L_{me} is displayed in Figure 8b. The flow transition between these two asymptotic regimes is well represented by the CorJet predictions. Figure 8b also includes recent data by Wang [51] on concentration measurements in the jet/wake transition covering a wide range of the pure wake. The Gaussian concentration width measurements b_c are plotted as b_c/λ (with $\lambda = 1.20$). These data agree well in trend, but seem to show in the pure wake range that – relative to the velocity data by Nickels and Perry [50] and the CorJet predictions – $\lambda > 1.20$ by some 20%, a fact that may be related to weakly turbulent, almost laminar conditions in the experiments in that range. Unfortunately, no simultaneous measurements on velocity and concentration distributions are available to date to reconcile this aspect.

For the cases of the advected line puff and thermal, respectively, the azimuthal shear mechanism is dominant and the average entrainment velocity u_e at the nominal jet width b is proportional to the transverse propagation velocity, $u_e \sim u_p$, in which $u_p = u_a(1 - \cos^2\theta_o \cos^2\sigma_o)^{1/2}$.

For the **advected line puff**, $u_e = \alpha_{puff}\, u_p$ with the puff entrainment coefficient $\alpha_{puff} = \alpha_4 = 0.5$ consistent with the basic work of Richards [52]. The asymptotic behavior for the advected puff case with a vertical transverse momentum component is given by the vertical rise $z \sim x^{1/3}$ and the dilution $S_c \sim z^3$. Data on advected line puffs can be found in the recent study of Chu [29] in which a special injection device was used to assure a discharge with zero excess longitudinal momentum M_{oe} but only vertical (i.e., $\sigma = 0°$) transverse momentum flux M_{ot}, see Equation (2), that defines the length scale $L_{mt} = M_{ot}^{1/2}/u_a$. Figure 9a shows the data on the normalized vertical trajectory z/L_{mt} and Figure 9b the normalized centerline dilution $S_c Q_o/(u_a L_{mt}^2)$ as a function of downstream distance x/L_{mt} together with CorJet predictions. Despite considerable data scatter because of the strongly fluctuating flow character the agreement is good. Furthermore, the experimental determination of centerline dilutions is somewhat tenuous due to the internal vortex structure leading to lower concentrations – and hence higher dilutions – along the centerline.

The **advected line thermal** has an average entrainment velocity $u_e = \alpha_{thermal}\, u_p$ for which the thermal entrainment coefficient $\alpha_{thermal} = \alpha_4 = 0.5$ is approximately equal to the puff values, again based on Richards' work that suggests roughly similar entrainment mechanisms for these flows. The asymptotic solutions are for by the vertical rise $z \sim x^{3/4}$ and the dilution $S_c \sim z^2$, respectively. Figure 10 shows the comparison with the advected thermal data of Fai [53]. Here lengths are normalized with L_b, see Equation (30), and the centerline dilution as $S_c Q_o/(u_a L_b^2)$. Again, despite the data scatter the agreement with model predictions is satisfactory both in trend and in magnitude.

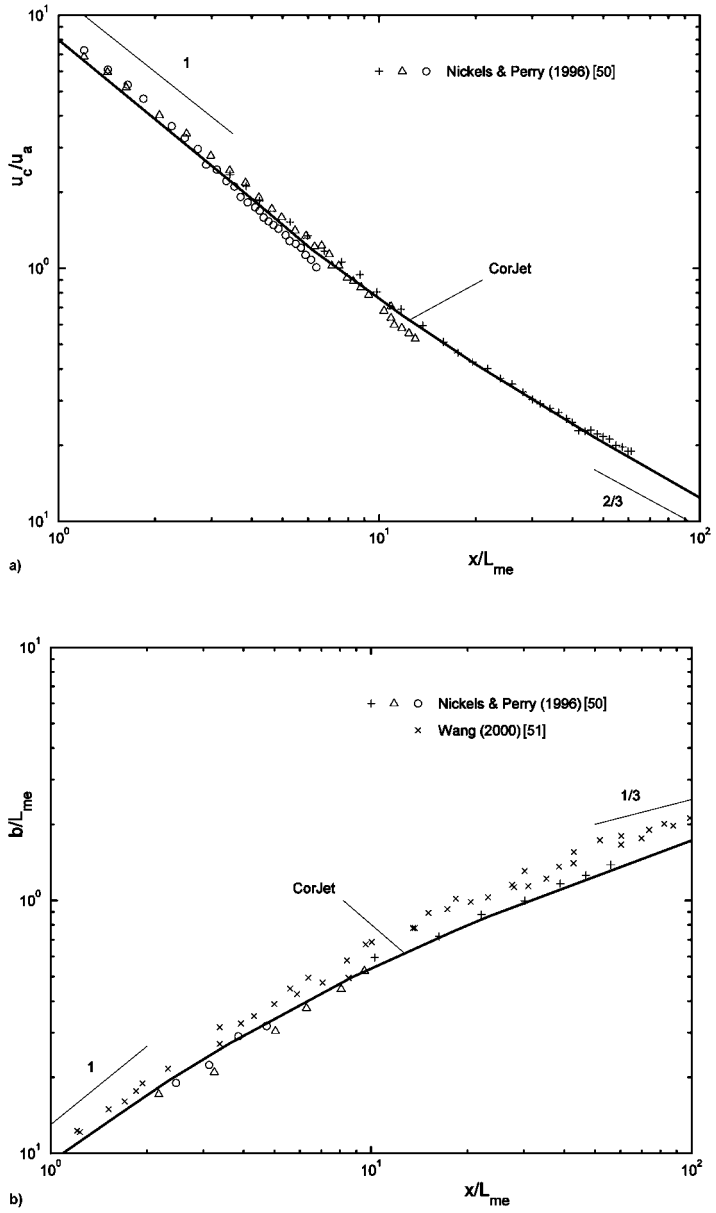

Figure 8. Jet/wake transition in ambient co-flow: Comparison of experimental data by Nickels and Perry [50] and Wang [51] with integral model predictions: (a) Decay of centerline velocity u_c/u_a, and (b) increase of jet width b/L_{me}, both as function of normalized axial distance x/L_{me}. Slopes indicate asymptotic behavior.

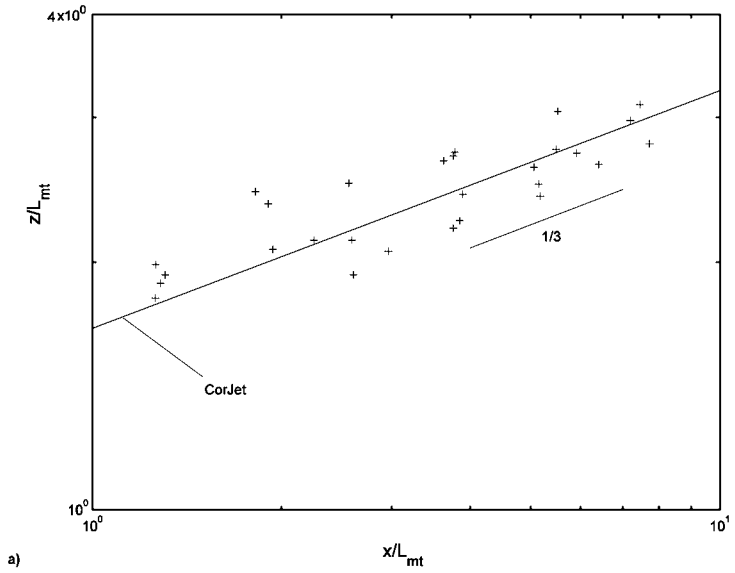

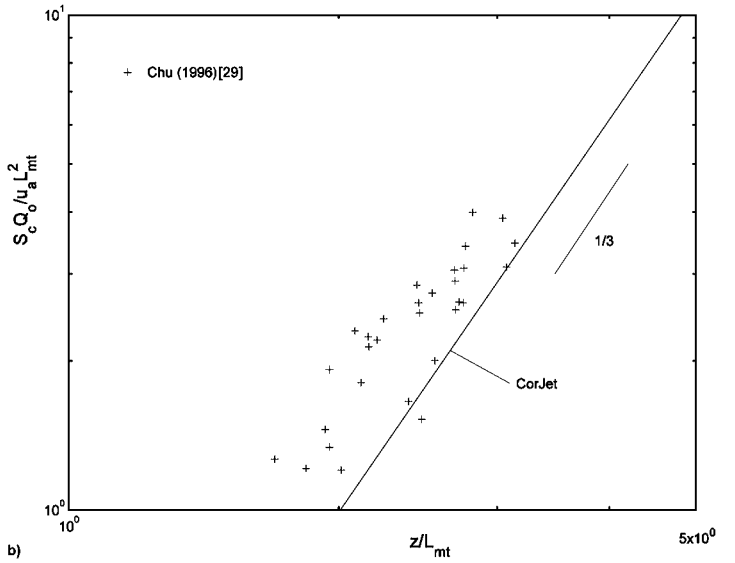

Figure 9. Advected line puff: Comparison of experimental data by Chu [29] with integral model predictions: (a) Vertical rise z/L_{mt}, and (b) normalized centerline dilution $S_c Q_o/(u_a L_{mt}^2)$, both as a function of downstream distance x/L_{mt}. Slopes indicate asymptotic behavior. Slopes indicate asymptotic behavior.

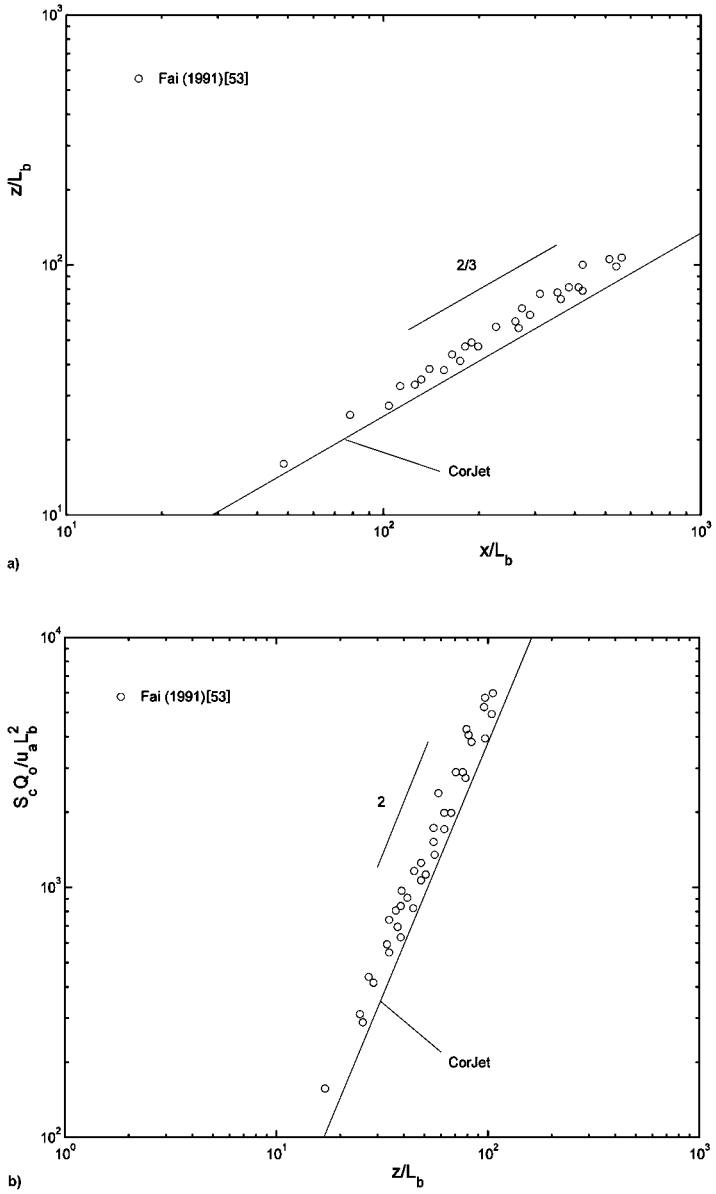

Figure 10. Advected line thermal: Comparison of experimental data by Fai [53] with integral model predictions: (a) Vertical rise z/L_b, and (b) normalized centerline dilution $S_c Q_o/(u_a L_b^2)$, both as a function of downstream distance x/L_b. Slopes indicate asymptotic behavior.

In summary, the above comparisons of the integral model with data for the five asymptotic cases show that the basic model assumptions and formulation are adequate for these limits and validate the set of model coefficients, Equation (29) (with the exception of c_D that will be addressed in the following). Of particular interest is the constant value of $\lambda = 1.20$ that seems to represent a good average over the complete range (with possibly slightly lower values for the plume and slightly higher values for the strongly advected cases). In any case, a model formulation that would include some variability of λ [32] seems hardly warranted in view of the data uncertainty on one hand and the good predictions of the present model on the other. The representation of the vortex pair structure for the advected line puff and thermal regimes by means of a Gaussian profile assumption also seems supported by the model predictions, in particular for such overall features as trajectories, widths and dilutions (see Figures 9 and 10).

Table I summarizes the analytical expressions for the five self-similar asymptotic regimes, based on the basic coefficients that have resulted from the above model validation.

In that context it is quite remarkable to note the differences between the pure wake with its transverse and the advected line puff with its azimuthal shear mechanism, respectively. The latter with its internal vortex structure seems about 75% more efficient in leading to entrainment and mixing. Thus, the crossflow component of the initial momentum flux plays a role not only in the discharge vicinity but continues to exert some influence also at larger distances in the strongly advected stages.

4.2. NON-EQUILIBRIUM BUOYANT JET FLOWS

General buoyant jet flows, often with complex three-dimensional trajectories, with variable ambient stratification and/or with crossflows, are in a non-equilibrium state lacking local self-similarity. As has been stated in Principle 2, the formulation of the transition functions for these non-equilibrium conditions cannot be derived from first principles. Thus, the adequacy of the present formulation for turbulent entrainment, Equation (20), and for the drag force, Equation (21), has to be guided largely by satisfactory data comparisons under a variety of transitional flow conditions. This is done in the following. Also, several limits of applicability (Principle 6) for the integral formulation are provided.

4.2.1. *Buoyancy-Induced Transitions in Stagnant Environment*

The **horizontal buoyant jet** ($\theta_o = 0°$) is one of the most common applications for aquatic discharges. Figure 11 shows the normalized vertical trajectory z/L_M as a function of x/L_M for a variety of experimental conditions with different Froude number F_o and in comparison the CorJet model predictions. The data scatter is typical for these experiments in which visual observations are used for the trajectory determination. The normalized centerline dilution S_c/F_o as a function of elevation

Table I. Equations for the Five Self-Similar Asymptotic Regimes of the Round Buoyant Jet.

Regime (all $\lambda = 1.20$)	Width b	Centerline velocity u_c or trajectory elevation z	Volume flux Q	Centerline dilution $S_c = c_o/c_c$	Remarks
Jet	$b = 2\alpha_{jet} x$	$u_c = \frac{1}{\sqrt{2\pi}\,\alpha_{jet}} \frac{M_o^{1/2}}{x}$	$Q = \sqrt{2\pi}\, 2\alpha_{jet} M_o^{1/2} x$	$S_c = \frac{\lambda^2}{1+\lambda^2} \frac{\sqrt{2\pi} 2\alpha_{jet}}{1+\lambda^2} \frac{M_o^{1/2} x}{Q_o}$	Assumes discharge in x-direction
$\alpha_{jet} = 0.055$	$b = 0.11\, x$	$u_c = 7.25 \frac{M_o^{1/2}}{x}$	$Q = 0.27 M_o^{1/2} x$	$S_c = 0.162 \frac{M_o^{1/2} x}{Q_o}$	
Plume	$b = \frac{6}{5}\alpha_{plume} z$	$u_c = \frac{1}{2}\left(\frac{25}{3\pi}\frac{1+\lambda^2}{\alpha_{plume}^2}\right)^{1/3} \frac{J_o^{1/3}}{z^{1/3}}$	$Q = \frac{6}{5}\left(\frac{9}{5}(1+\lambda^2)\pi^2\alpha_{plume}^4\right)^{1/3} J_o^{1/3} z^{5/3}$	$S_c = \frac{\lambda^2}{1+\lambda^2}\frac{6}{5}\left(\frac{9}{5}\frac{\lambda^6}{(1+\lambda^2)^2}\pi^2\alpha_{plume}^4\right)^{1/3} \frac{J_o^{1/3} z^{5/3}}{Q_o}$	
$\alpha_{plume} = 0.083$	$b = 0.10\, z$	$u_c = 4.9 \frac{J_o^{1/3}}{z^{1/3}}$	$Q = 0.152\, J_o^{1/3} z^{5/3}$	$S_c = 0.090 \frac{J_o^{1/3} z^{5/3}}{Q_o}$	
Wake	$b = \left(\frac{3\alpha_{wake}}{2\pi}\right)^{1/3} \frac{M_{oe}^{1/3} x^{1/3}}{u_a^{2/3}}$	$u_c = \frac{1}{\pi}\left(\frac{2\pi}{3\alpha_{wake}}\right)^{2/3} \frac{M_{oe}^{1/3} u_a^{1/3}}{x^{2/3}}$	$Q = 2\pi\left(\frac{3\alpha_{wake}}{2\pi}\right)^{2/3} \frac{M_{oe}^{2/3} x^{2/3}}{u_a^{1/3}}$	$S_c = \lambda^2\pi\left(\frac{3\alpha_{wake}}{2\pi}\right)^{2/3} \frac{M_{oe}^{2/3} x^{2/3}}{u_a^{1/3} Q_o}$	
$\alpha_{wake} = 0.11$	$b = 0.37 \frac{M_{oe}^{1/3} x^{1/3}}{u_a^{2/3}}$	$u_c = 2.27 \frac{M_{oe}^{1/3} u_a^{1/3}}{x^{2/3}}$	$Q = 0.88 \frac{M_{oe}^{2/3} x^{2/3}}{u_a^{1/3}}$	$S_c = 0.63 \frac{M_{oe}^{2/3} x^{2/3}}{u_a^{1/3} Q_o}$	
Advected Line Puff	$b = \left(\frac{3\alpha_{puff}}{4\pi}\right)^{1/3} \frac{M_{ot}^{1/3} x^{1/3}}{u_a^{2/3}}$	$z = \left(\frac{6}{\pi\alpha_{puff}^2}\right)^{1/3} \frac{M_{ot}^{1/3} x^{1/3}}{u_a^{2/3}}$	$Q = \left(\sqrt{\frac{\pi}{2}} 3\alpha_{puff}\right)^{2/3} \frac{M_{ot}^{2/3} x^{2/3}}{u_a^{1/3}}$	$S_c = \frac{\lambda^2}{2}\left(\sqrt{\frac{\pi}{2}} 3\alpha_{puff}\right)^{2/3} \frac{M_{ot}^{2/3} x^{2/3}}{u_a^{1/3} Q_o}$	Assumes transverse momentum flux M_{ot} in z-direction
$\alpha_{puff} = 0.5$	$b = 0.49 \frac{M_{ot}^{1/3} x^{1/3}}{u_a^{2/3}}$	$z = 1.96 \frac{M_{ot}^{1/3} x^{1/3}}{u_a^{2/3}}$	$Q = 1.52 \frac{M_{ot}^{2/3} x^{2/3}}{u_a^{1/3}}$	$S_c = 1.10 \frac{M_{ot}^{2/3} x^{2/3}}{u_a^{1/3} Q_o}$	
Advected Line Thermal	$b = \left(\frac{3\alpha_{thermal}}{8\pi\lambda}\right)^{1/3} \frac{J_o^{1/3} x^{2/3}}{u_a}$	$z = \left(\frac{3}{\pi\lambda\alpha_{thermal}^2}\right)^{1/3} \frac{J_o^{1/3} x^{2/3}}{u_a}$	$Q = \left(\sqrt{\frac{\pi}{2}}\frac{3\alpha_{thermal}}{2\lambda}\right)^{2/3} \frac{J_o^{2/3} x^{4/3}}{u_a}$	$S_c = \frac{\lambda^2}{2}\left(\sqrt{\frac{\pi}{2}}\frac{3\alpha_{thermal}}{2\lambda}\right)^{2/3} \frac{J_o^{2/3} x^{4/3}}{u_a Q_o}$	
$\alpha_{thermal} = 0.5$	$b = 0.37 \frac{J_o^{1/3} x^{2/3}}{u_a}$	$z = 1.47 \frac{J_o^{1/3} x^{2/3}}{u_a}$	$Q = 0.85 \frac{J_o^{2/3} x^{4/3}}{u_a}$	$S_c = 0.61 \frac{J_o^{2/3} x^{4/3}}{u_a Q_o}$	

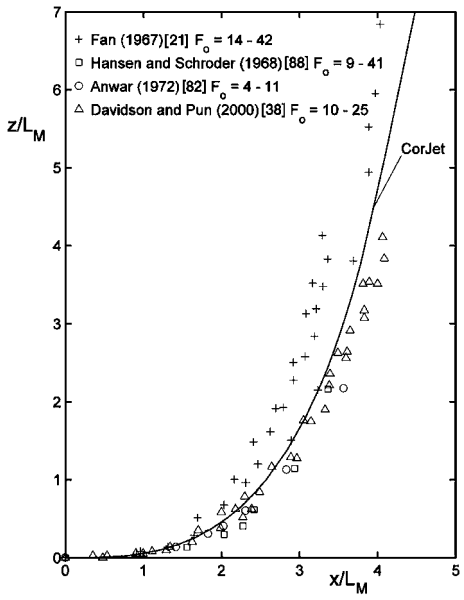

Figure 11. Horizontal buoyant jet in stagnant ambient: Normalized vertical trajectory z/L_M as a function of x/L_M.

z/L_M is displayed in Figure 12. For large z/L_M the approach to the pure plume behavior $S_c \sim z^{5/3}$ (see Figure 6) is evident. The integral model seems to provide a satisfactory transition behavior as can be seen from both figures.

The **vertical negatively buoyant jet** ($\theta_o = 90°$, $g'_o < 0$) represents a strongly anomalous flow situation. During the initial stages before reversal (i.e., the maximum rise) has been reached the flow direction (generally given by the component $\sin\theta$) is opposite to the direction of buoyant acceleration, so that the parameter combination $F_\ell^2/\sin\theta < 0$. Given Equation (20) this means that the entrainment rate falls below that of the jet because work is being done against gravity consistent with the earlier mentioned models of Fox [33] and Jirka and Harleman [49]. As the jet decelerates and approaches reversal, then stagnates (i.e., $F_\ell^2/\sin\theta = 0$) and finally undergoes downward acceleration until it reaches asymptotically the pure plume stage, the entrainment transitions are largely unresolved. A linear transition between the decelarating and accelerating stages of the jet motion is assumed in the integral model formulation. The complete entrainment functionality is shown in Figure 13. The range of the positively buoyant jet/plume transition is well validated by the direct measurements of Wang and Law [32] that have been discussed in the preceding Subsection. A detailed testing of this proposed relationship for the negatively buoyant range is impossible as precise data along the jet path have not been measured to date. Furthermore, the reversing jet is re-entraining to some degree its own mixed fluid, leading to a strong fluctuations during the fountain-like reversal [54]. Various investigators have measured the height of rise $Z_{\max}$ of the decelerating

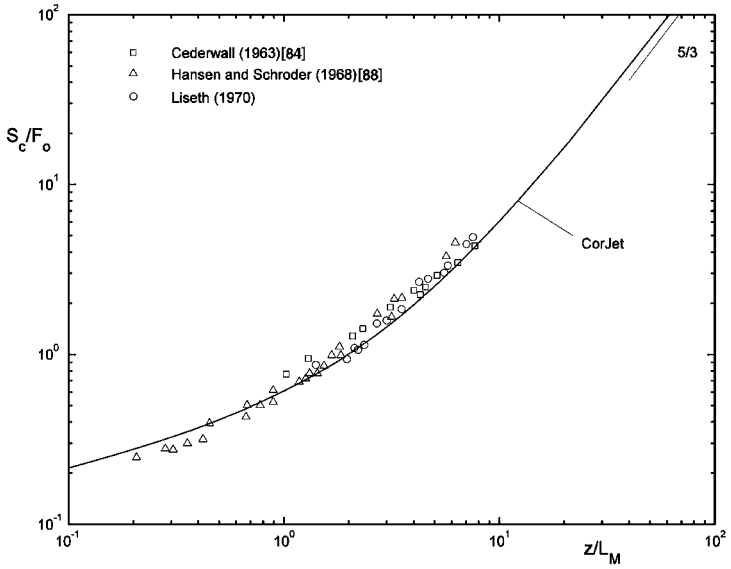

Figure 12. Horizontal buoyant jet in stagnant ambient: Normalized centerline dilution S_c/F_o as a function of elevation z/L_M.

buoyant jet, usually interpreted as the maximum visual level. Recent data by Zhang and Baddour [55] are shown in Figure 14 in normalized form $Z_{\max}/D$ as a function of discharge Froude number F_o (in which the absolute value of g'_o is used). For comparison the CorJet predictions are given in which $Z_{\max}$ is taken as the sum of trajectory elevation $z_{\max}$ and visual boundary $\sqrt{2}b$, i.e., $Z_{\max} = z_{\max} + \sqrt{2}b$. The CorJet predictions are in good agreement with the data and given by the functional relation

$$Z_{\max} = 2.2L_M \tag{33}$$

Other experimental studies [54, 56] have led to similar values for the constant in this equation, ranging from 1.7 to 3.2 [55] and reflecting some judgement in the interpretation of $Z_{\max}$. CorJet also predicts a normalized minimum dilution at the reversal level

$$S_m/F_o = 0.24 \tag{34}$$

that is in excellent agreement with the data (constant 0.23) by Abraham [56]. On the other hand, the CorJet model fails to predict the data trend observed by Zhang and Baddour for low $F_o < 5$ that show a substantial a substantial decrease of $Z_{\max}$ (up to 50% as $F_o \leqslant 1$). Clearly, that is related to the re-entrainment after reversal of strongly negatively buoyant fluid for these weakly mixing situations, see Equation (34), that is not recognized in the model formulation.

Overall, the vertical negatively buoyant jet represents one extreme case of jet behavior that stretches in the reversal stage the underlying boundary layer assumption (Principle 3). Nevertheless, a reasonably satisfactory model performance for

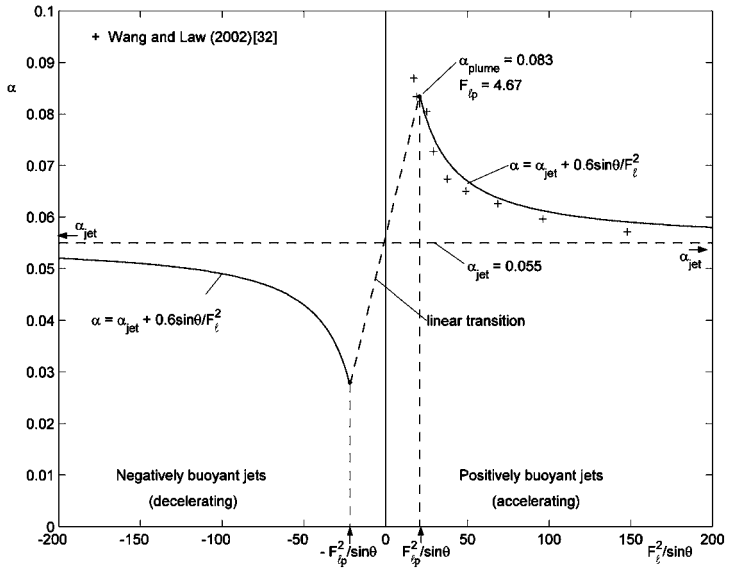

Figure 13. Behavior of the buoyant jet entrainment function in stagnant ambient conditions covering the complete transition range of local negative and positive buoyancy, respectively.

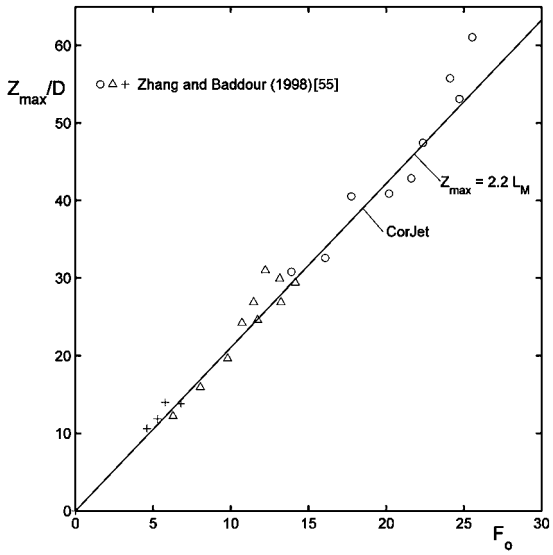

Figure 14. Vertical negatively buoyant jet in stagnant ambient: Comparison of integral model predictions with experimental data by Zhang and Baddour [55] for the normalized vertical rise form $Z_{\max}/D$ as a function of discharge Froude number F_o.

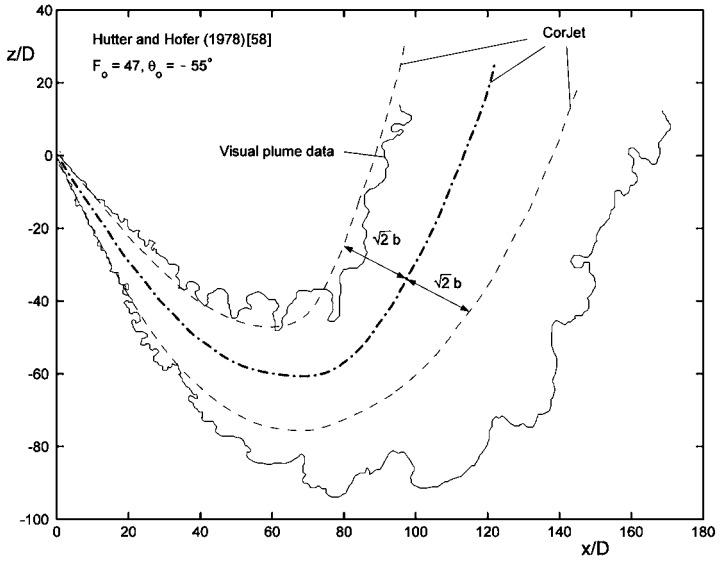

Figure 15. Inclined negatively buoyant jet in stagnant ambient: Comparison of integral model predictions with experimental data by Hutter and Hofer [58] for the two-dimensional trajectory, z/D versus x/D.

this situation is an important basis for other such near-extreme situations such as strongly inclined negatively buoyant jets (a frequent application is the disposal of brines from desalination plants). For example, the case of $\theta_o = 60°$ has been studied by Roberts and Toms [57]. They report a maximum jet elevation $Z_{\max} = 2.2L_M$ while CorJet predicts $Z_{\max} = 1.9L_M$, both values not substantially different from the vertical case , Equation (33), keeping in mind the typical variability. The minimum dilution at that level is measured as $S_m/F_o = 0.38$ compared to the CorJet prediction $S_m/F_o = 0.29$, these higher values relative to Equation (34) arise because of the longer jet path. No detailed data for the jet trajectory have been reported by Roberts and Toms [57]; however, the comparatively similar case of $\theta_o = 55°$ has been measured by Hutter and Hofer [58], and the model comparison is given in Figure 15 showing good agreement for jet trajectory and visual width $\sqrt{2}b$.

Momentum sources in form of **pure jets in linearly stratified environments** ($J_o = 0$, $\varepsilon > 0$) provide an important case for the transition of jet flows to buoyant collapse motion as internal density currents. **Horizontal momentum injections** ($\theta_o = 0°$) have been studied by Roberts *et al.* [59] who observed the variation of normalized centerline dilution $S_c L_Q/L'_m$ as function of distance x/L'_m as plotted in Figure 16. The data show an essentially linear increase of dilution corresponding to the equation for a simple jet $S_c = 0.162\, x/L_Q$ (see Table 1) in an initial region $x/L'_m \leqslant 5$ and an essentially constant dilution level $S_c L_Q/L'_m \simeq 0.8$ beyond that distance. This lack of further mixing indicates a suppression of jet entrainment and also coincides with strong lateral spreading (see also visual observations by

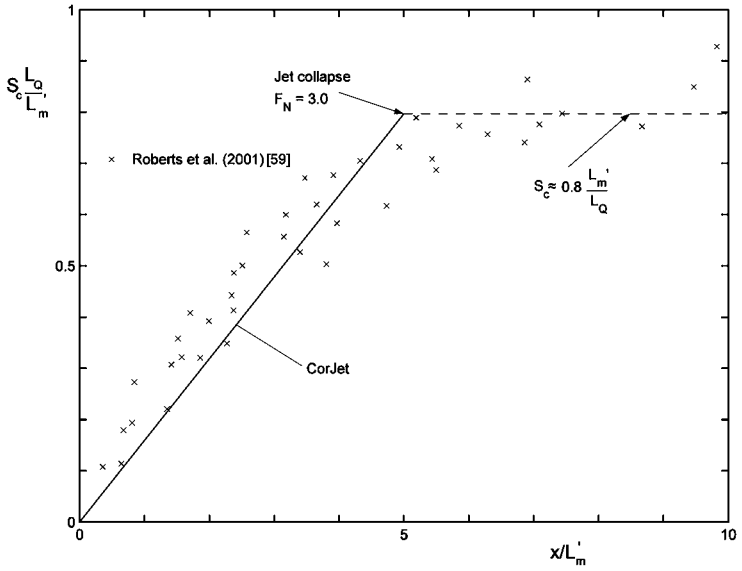

Figure 16. Horizontal momentum sources in stagnant linearly stratified environment: Comparison of integral model predictions with experimental data by Roberts *et al.* [59] for normalized centerline dilution $S_c L_Q / L'_m$ as function of distance x/L'_m.

Roberts and Matthews [60]. In sum, the jet undergoes a collapse in the stratified environment. An estimate for the collapse transition at which the integral jet model cease to be valid can be derived: Following Akar and Jirka [61] the lateral spreading front velocity u_f of a mixed region of vertical half-height h in a linear stratification with buoyancy frequency $N = \sqrt{\varepsilon}$ is given

$$u_f = \left(\frac{2}{3C_D}\right)^{1/2} Nh \tag{35}$$

in which C_D is a frontal drag coefficient in the inertial spreading stage [62] with a value $C_D \simeq 1.2$ for internal density currents, so that $u_f \simeq 0.75Nh$. The horizontal buoyant jet that is advancing with a mean velocity proportional to its centerline velocity u_c will undergo increasing lateral collapse whenever $u_f \approx cu_c$ where c is a fraction expected to be less than unity. Defining a local Froude number F_N [63] for the jet in continuous stratification

$$F_N = \frac{u_c}{Nb}, \tag{36}$$

the condition for jet collapse becomes

$$F_N \simeq F_{Ncrit} \tag{37}$$

in which the local scales $h \approx b$. Data comparisons (see the following figures) suggest the fractional value $c \approx 0.25$ so that $F_{Ncrit} \approx 3.0$. The comparison in

Figure 16 of the CorJet model predictions with the data of Roberts *et al.* support the adequacy of the transition estimate, Equation (37).

Non-horizontal momentum injections ($|\theta_o| > 0°$) as well as **buoyant jet sources** ($|J_o| > 0$) in stagnant stratification create yet more complex transition conditions in which the jet motion first experiences some upward or downward motion until it reaches – after some overshoot to a maximum or minimum height – a terminal level where the centerline density is equal to the ambient density and the lateral collapse in form of an internal density current commences. An integral jet model formulation will – in the absence of an adequate transition cutoff – predict an infinite number of oscillations of the round jet about the terminal level as has been noted in earlier studies. This is unrealistic as the models do not recognize the jet collapse physics. Evaluation of the detailed experimental data of several investigators and attendant model comparisons suggest the following rules for terminal layer transition and hence end of the jet region:

(1) Transition occurs at the second buoyancy reversal (i.e., change of sign of the local centerline buoyancy as defined in Equation (5)) of the buoyant jet motion. For strong momentum sources this rule, typically, also satisfies the collapse condition, Equation (37).

(2) Transition can already occur (i) at the first buoyancy reversal if for strongly buoyant flows a more restrictive collapse condition, $F_N \leqslant 0.25 F_{Ncrit}$, is met, or (ii) at the maximum or minimum rise level if the collapse condition, Equation (37), is met there, or (iii) at the first buoyancy reversal if the jet motion has already undergone through a maximum or minimum rise level and then meets a more relaxed condition, $F_N \leqslant 2F_{Ncrit}$.

In Figure 17, the data by Fan [21] for a strongly buoyant flow, $F_o = 9.1$, $T = 48$, $\theta_o = 45°$, in which T is a stratification parameter $T = g'_o/(\varepsilon D)$, are compared with the CorJet model. The data in form of tracings of photographic plume observations clearly show the unsteady behavior of the jet collapse and internal density current formation. In the initial phase the buoyant jet overshoots to the maximum height and then falls back to the terminal level. This behavior is well predicted in trajectory and visual width $\sqrt{2}b$ by the integral model that indicates the two buoyancy reversals and the final value $F_N = 3.1$. At later stages in the experiment, however, the blocking and feedback effect that is typical for internal density currents [63] makes itself evident: Because of the reduced mixing the observed terminal level rises somewhat and the layer increases in thickness over time. Clearly, these effects are beyond the jet regime. These aspects are further illustrated in Figures 18 for (a) moderately buoyant jet ($F_o = 21$, $T = 107$, $\theta_o = 43.6°$), and (b) horizontal weakly buoyant jet ($F_o = 60$, $T = 510$, $\theta_o = 0°$). Generally, the terminal layer that is observed for sufficiently long times lies in the region between the maximum rise and the predicted terminal level. This unsteady effect is, of course, a special characteristic of the stagnant stratified blocking effect. It is less severe for cases of stratification with crossflow as discussed further below. The terminal level rules proposed above seem adequate even in this extreme situation. Data by different

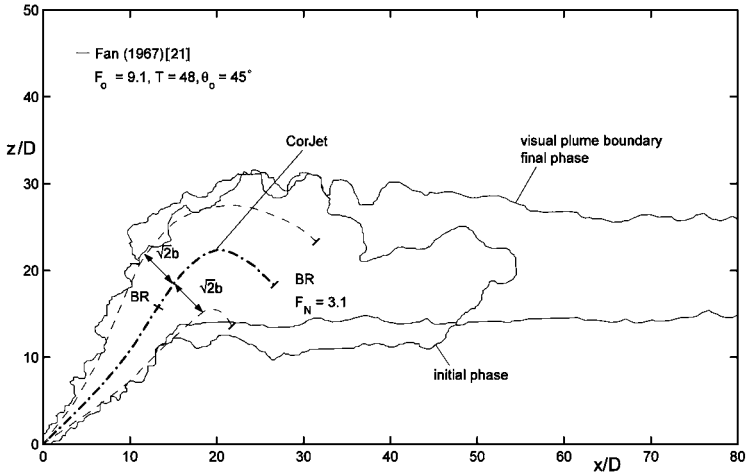

Figure 17. Buoyant jet in stagnant linearly stratified environment: Comparison of integral model predictions with experimental data by Fan [21] for the two-dimensional trajectory. The two tracings of plume outlines indicate the early and later stages of terminal layer formation. The CorJet predictions include the visual plume width $\sqrt{2}b$, locations of buoyancy reversal (BR), and values of the local Froude number F_N, respectively.

investigators [58] given in Figure 19 actually show a slightly different trend as the observed terminal layer lies somewhat below the prediction (Figure 19a). This may be due to inaccuracies in determining the weak ambient stratification. The predicted mixing in this momentum dominated case ($F_o = 34$, $T = 920$, $\theta_o = 0°$) is well predicted, however (Figure 19b).

Lastly, the CorJet predictions can be compared with data for vertical jet and plume motions ($\theta_o = 90°$), respectively, that have been cited in the literature [31, 64] even though detailed observations are missing. For vertical pure jets in stratification, CorJet predicts a maximum rise level $Z_{\max} = z_{\max} + \sqrt{2}b$ as $Z_{\max}/L'_m = 3.3$ and a terminal level z_t as $z_t/L'_m = 1.5$, respectively. The experimentally observed levels are 3.8 to 4.0 and 2.6, respectively. For a plume in stratification the CorJet predictions give $Z_{\max}/L'_b = 4.1$ and $z_t/L'_b = 2.5$, while the data indicate again 3.8 to 4.0 and 2.6, respectively. Again, given the usual fluctuations and unsteadiness in the experiments this agreement is satisfactory which incidentally is another evidence for the adequacy of the proposed entrainment formulation depicted in Figure 13. The fact that the reported terminal levels under these stagnant conditions are somewhat higher with the predictions is consistent with the earlier discussion (see Figure 17).

4.2.2. *Buoyant Jet Transitions in Flowing Unstratified Environment*

The **non-buoyant jet discharging into transverse crossflow** is a classical well-studied case of the interaction of a momentum source with an ambient flow. In the following all results are displayed in the vertical x-z plane (so that $\theta_o = 90°$) even

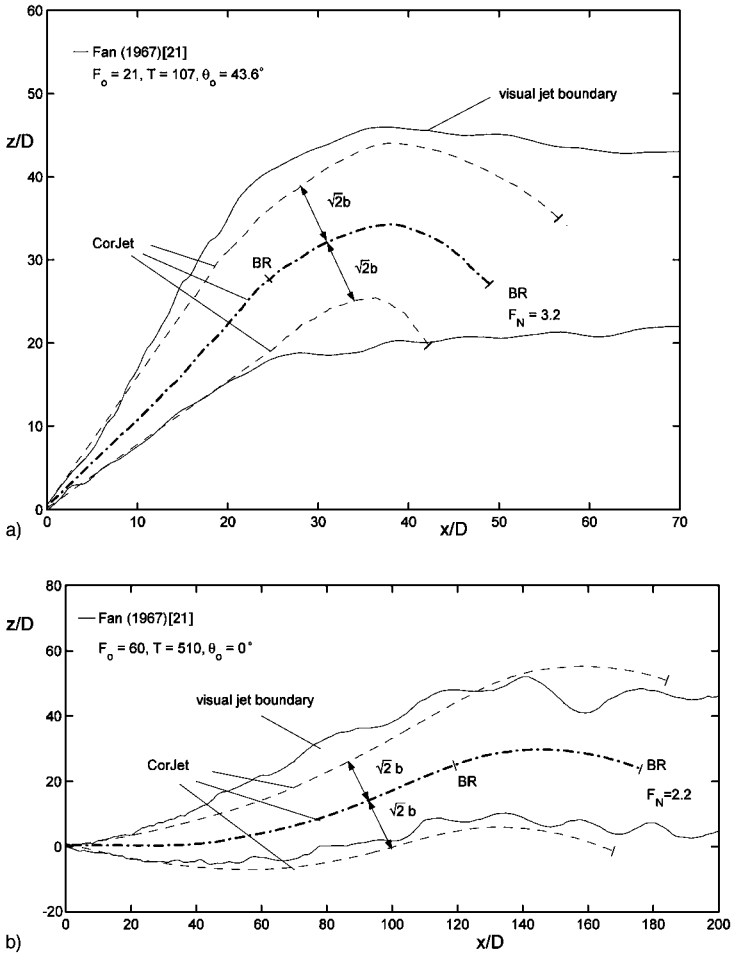

Figure 18. Buoyant jet in stagnant linearly stratified environment: Comparison of integral model predictions with experimental data by Fan [21] for the two-dimensional trajectory: (a) Inclined moderately buoyant jet, (b) horizontal weakly buoyant jet. For symbols see Figure 17.

though gravity is immaterial in these cases. Figure 20 shows the data for centerline trajectories obtained from photographic observations by Pratte and Baines [65] compared to integral model predictions. The agreement is satisfactory for a wide range of discharge/crossflow velocity ratios R, Equation (22). A large number of laboratory measurements for jet trajectories as well as dilutions were performed by Fan [21] and Wright [22]. Their aggregate data covering a range of source effects, L_Q/L_m from 0.01 to 0.3, are shown in normalized form in Figure 21 for trajectories z/L_m and in Figure 22 for centerline dilution $S_c L_Q/L_m$, respectively. The corresponding CorJet predictions are given simply for a small source condition, $L_Q/L_m \to 0$. Some of the data scatter is clearly related to the source effect, a larger degree of variability relates, however, to ambiguities in the determination of

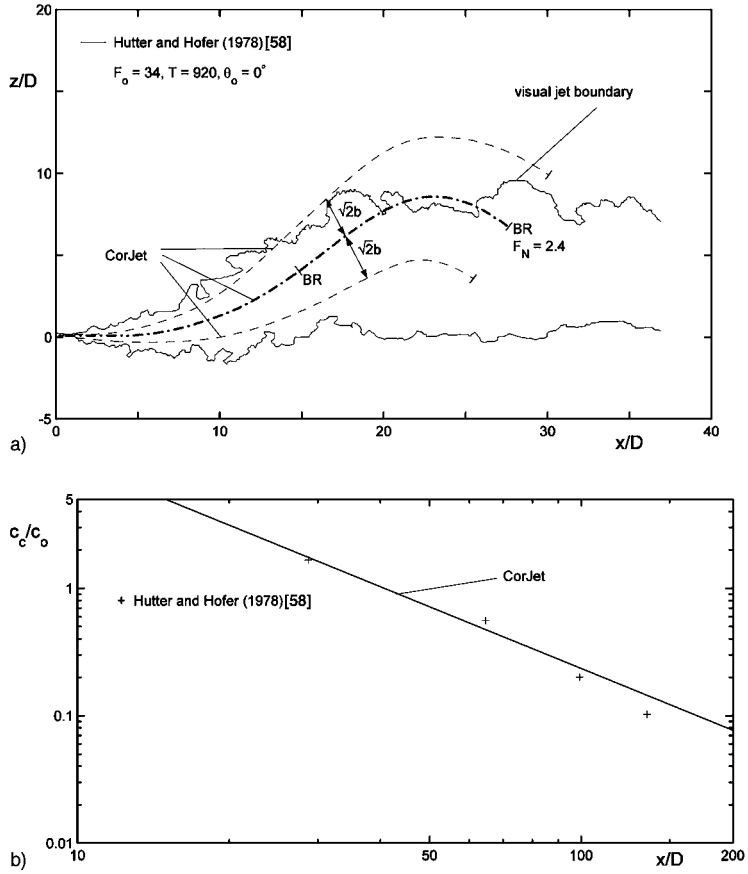

Figure 19. Buoyant jet in stagnant linearly stratified environment: Comparison of integral model predictions with experimental data by Hutter and Hofer [58] for a horizontal weakly buoyant jet: a) two-dimensional trajectory, b) decay of normalized centerline concentration c_c/c_o. For symbols see Figure 17.

the centerline trajectory as well as minimum dilutions. The trajectories in Figure 21 were obtained from maximum concentration measurements on the centerplane, which typically lie some 20% above the photographic data (as was used by Pratte and Baines [65], see Figure 20). The measured minimum dilutions on the centerplane S_{CP} are typically a factor of 1.7 higher than the minimum dilutions in the vortex cores S_{VC} [66] which are represented by the value S_c in the integral model formulation. With these aspects in mind the comparisons in these two figures indicate satisfactory model performance, including the correct asymptotic behavior for dilution, $S_c \sim z^2$ (from Table I).

It can be noted in the logarithmic plot of Figure 21 that the trajectory behavior in the strongly deflected puff stage deviates below a slope of 1/3 (see Table I). This is due to the drag force effect that diminishes the vertical rise from what might be expected from simple dimensional reasoning. This deviation was already evident

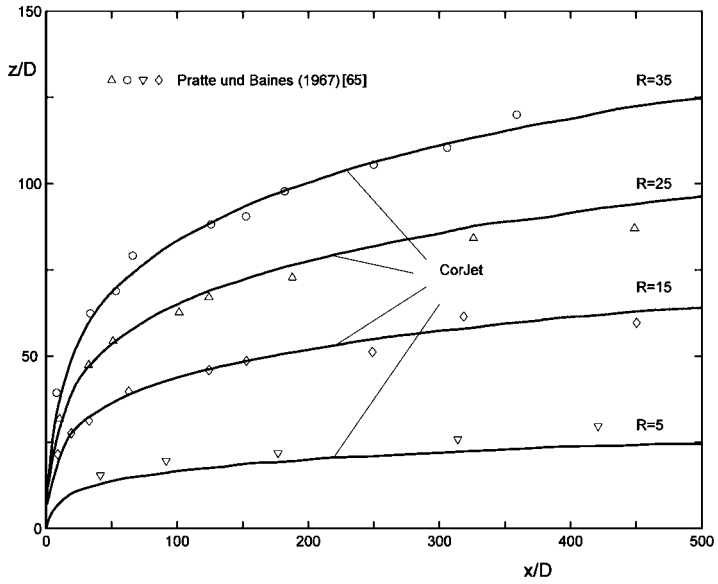

Figure 20. Non-buoyant jets in transverse crossflow: Comparison of integral model predictions with experimental data by Pratte and Baines [65] for two-dimensional trajectories with different discharge/crossflow velocity ratios *R*.

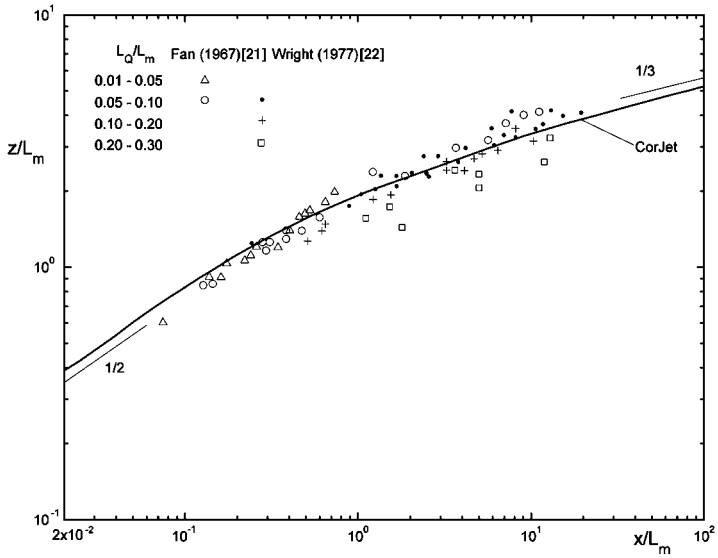

Figure 21. Non-buoyant jets in transverse crossflow: Normalized two-dimensional trajectories, z/L_m *versus* x/L_m. Slopes indicate exponents for power laws from dimensional analysis in the weakly and strongly deflected stages, respectively.

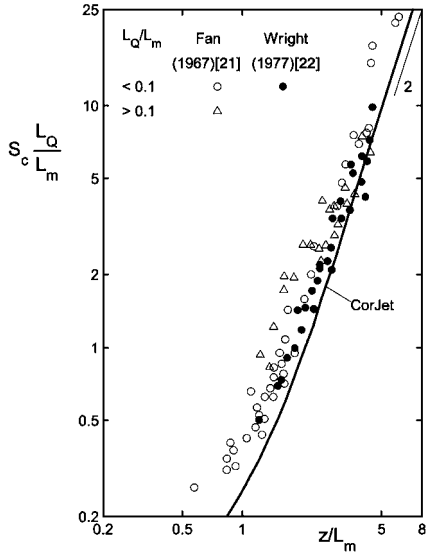

Figure 22. Non-buoyant jets in transverse crossflow: Normalized centerline dilution $S_c L_Q/L_m$ as a function of transverse distance z/L_m. Measured dilutions represent minimum values on the jet centerplane S_{CP}. Slopes indicate exponents for power laws from dimensional analysis in the weakly and strongly deflected stages, respectively.

in Figure 9a. The weakly deflected jet phase agrees well with dimensional analysis, $z \sim x^{1/2}$ [22]. Typically the transition from the weak to the strong deflection regime occurs at a transverse distance $z \sim L_m$. At that stage the integral model indicates a maximum local ratio of drag force F_D (Equation (21)) to entrainment force Eu_a of about 0.5. While this ratio is smaller in the initial and final stages of deflection, respectively, it indicates the relative important contribution of the drag force mechanism toward overall jet behavior. The necessity and sensitivity of the drag force term is further tested by assigning variable values of c_D in the model and evaluating the effect on the trajectory in the bent-over stage, ($x/L_M > 1$ (see Figure 21): Omitting the drag force ($c_D = 0$) predicts a trajectory that is elevated by a factor of 1.2 in the entire bent-over stage, while doubling its contribution ($c_D = 2 \times 1.3$) provides a trajectory a factor 0.88 lower. These results confirm that the drag force mechanism must be necessary part of an integral model formulation for jets in crossflow, a fact that is suggested more fundamentally by the recent detailed data on the deflection dynamics (see Section 3.3).

Jets discharging at **oblique angles** into crossflow have been studied by Margason [67] and Chu [66] among others. Figure 23 gives data for a 60° transverse angle θ_o discharging along ($\sigma_o = 0°$) or against ($\sigma_o = 180°$) the ambient flow at different velocity ratios R. The data, though limited to the discharge vicinity, support the model predictions. The **opposing jet** ($\theta_o = 0°$,$\sigma_o = 180°$) provides an extreme test of the model formulation as the jet loses near the point of maximum upstream penetration $-x_p$ its boundary layer character. Figure 24 compares the

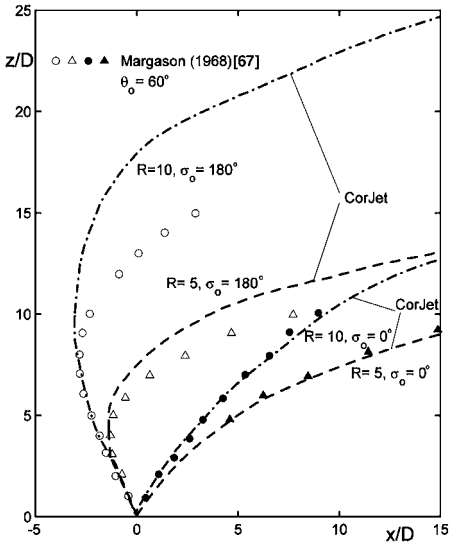

Figure 23. Non-buoyant jets discharging at oblique angles into or against ambient flow: Comparison of integral model predictions with experimental data by Margason [67] for normalized two-dimensional trajectories, z/D *versus* x/D.

model predictions with the data of Chan and Lam [68] for $R = 15$ who measured the decay of absolute centerline velocity $(u_c - u_a)/U_o$ and of visual width $\sqrt{2}b/D$ as a function of upstream distance $-x/D$. The data indicate centerline velocity stagnation at $-x_p/D \simeq 38.5$ while CorJet predicts a value of about 40. Scaled by the jet/crossflow length scale L_m the penetration distance is

$$\frac{-x_p}{L_m} = 3.0, \tag{38}$$

which is in close agreement with additional work by Yoda and Fiedler [69] that suggests a constant of 3.1. The data as well as the predictions of visual width show a non-linear growth up to a distance of about 2/3 of the penetration distance. After that the model predictions diverge as the jet enters into the stagnation region and ceases its boundary layer nature.

The **vertical buoyant jet into crossflow** ($J_o > 0$, $\theta_o = 90°$) is a very common environmental occurrence as chimney or stack emissions into the atmosphere. A typical laboratory study [21] with a laminar crossflow – the source being towed in these instance – is shown in Figure 25 as the visual plume outline as an indicator for the two-dimensional trajectory (Figure 25a), and as measurements of half-width $b_{1/2}/D$ (corresponding to $0.83b$ for the Gaussian profile) and minimum dilution in the vortex cores of the bent-over stage S_{VC} as a function of distance along the buoyant jet path s/D, both as indicators of mixing (Figure 25b). The agreement with the integral model is excellent for this case, supporting once more the notion that the minimum dilution in the vortex cores S_{VC} is well represented by the centerline dilution S_c of the Gaussian profile integral model, as has been

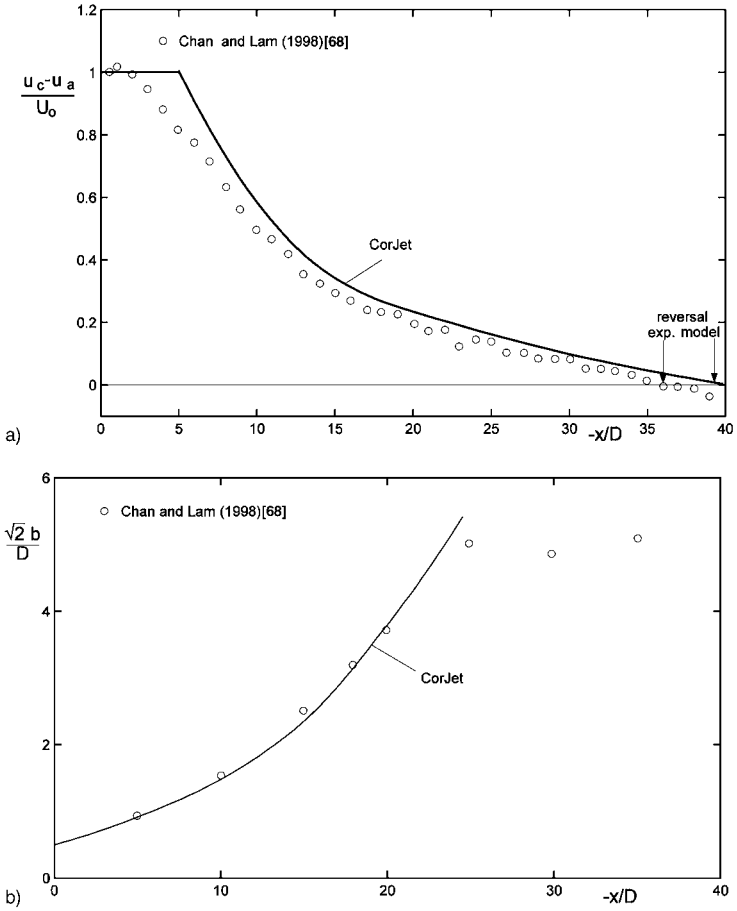

Figure 24. Opposing non-buoyant jets against ambient flow: Comparison of integral model predictions with experimental data by Chan and Lam [68]: (a) Decay of absolute centerline velocity $(u_c - u_a)/U_o$, (b) growth of visual jet width $\sqrt{2}b/D$, both as a function of upstream distance $-x/D$.

noted above. The observed and predicted trajectories for a wider range of flow conditions ($F_o = 20$, $R = 4$ to 16, or alternatively a range of the length scale ratio $L_m/L_b = (\pi/4)^{1/4} F_o^2/R^2 = 1.5$ to 24) are displayed in Figure 26. The internal transition in flow regimes from initial momentum dominated to final buoyancy-dominated regimes is not evident in these summary displays. This is better seen in the double-logarithmic representation of Figure 27 that shows data from Fan [21] and Wright [22] for the buoyancy-dominated regimes, analogous to Figure 21 for the momentum-dominated regimes. The data indicate a transition from a weakly-bent, $z \sim x^{3/4}$, to a strongly-bent region, $z \sim x^{2/3}$ (see Table I), as obtained from dimensional analysis. The integral model represents this transition well, but once again shows a slightly increased bending (or diminished rise) in the latter phase

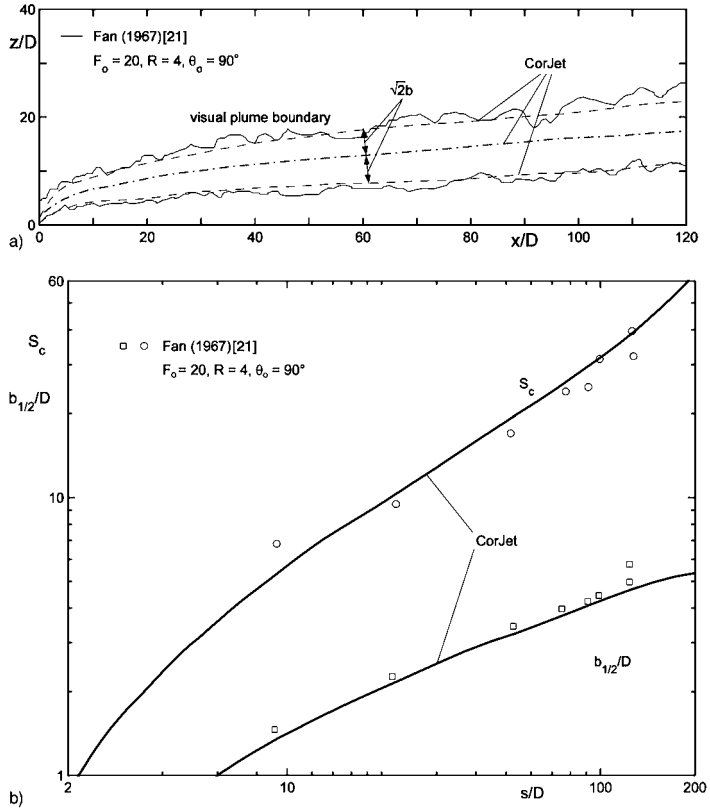

Figure 25. Vertical buoyant jet into crossflow: Comparison of integral model predictions with laboratory data by Fan [21]: (a) Vertical trajectory, z/D *versus* x/D, including visual plume width, (b) decay of normalized centerline concentration c_c/c_o and half-velocity width $b_{1/2}/D$ as function of distance along the buoyant jet path s/D.

due to the drag force effects as discussed above. The accompanying results for the normalized dilution $S_c L_Q L_m / L_b^2$ as function of vertical rise z/L_b are shown in Figure 28 using the data of Cheung [70]. The agreement is excellent in the weakly-bent stage with Gaussian cross-section for which dimensional analysis [22] yields for the dilution, $S_c \sim z^{5/3}$. For the strongly-bent stage with the double-vortex structure the model agrees in trend, $S_c \sim z^2$, but the data lie a certain factor (about 2) higher which is to be expected as the measurements give the minimum dilution on the centerplane S_{CP} as has been explained above.

The model results for a **co-flowing buoyant jet** ($J_o > 0$, $\theta_o = 0°$, $\sigma_o = 0°$) are compared in Figure 29 with the data of Ayoub [71] indicating both the trajectory rise as well as the concentration decay. The measurements by Davidson *et al.* [72] on the detailed entrainment patterns for this buoyant jet configuration in a weak crossflow are also of interest here: they clearly support the additive effects in the entrainment flow fields as specified in the entrainment formulation, Equation 20.

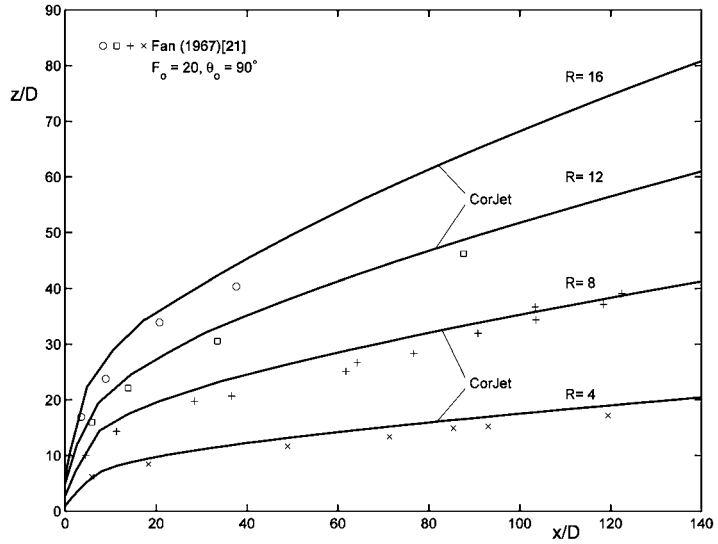

Figure 26. Vertical buoyant jets into crossflow: Comparison of integral model predictions with experimental data by Fan [21] for two-dimensional trajectories with a discharge Froude number $F_o = 20$ and variable discharge/crossflow velocity ratios $R = 4$ to 16.

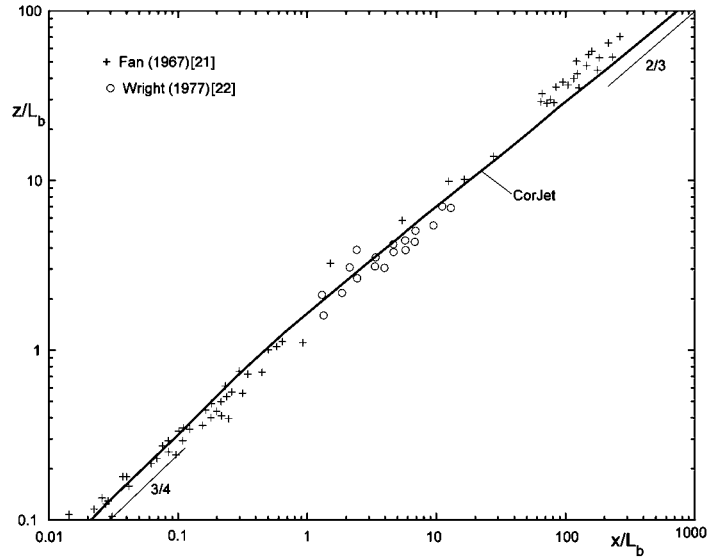

Figure 27. Vertical buoyant jets into crossflow: Normalized two-dimensional trajectories, z/L_b versus x/L_b. Slopes indicate exponents for power laws from dimensional analysis in the weakly and strongly deflected stages, respectively.

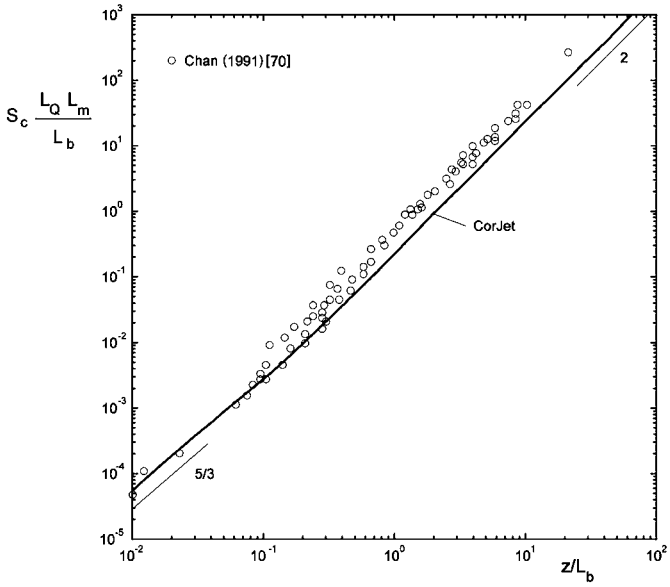

Figure 28. Vertical buoyant jets into crossflow: Normalized centerline dilution $S_c L_Q L_m / L_b^2$ as function of vertical rise z/L_b. Measurements values in the strongly deflected stage are minimum dilutions in the centerplane S_{CP}. Slopes indicate exponents for power laws from dimensional analysis in the weakly and strongly deflected stages, respectively.

Lastly, data for several cases of **negatively buoyant jets into crossflow** ($J_o < 0$, $\theta_o > 0°$, $\sigma_o = 0°$) are considered in Figures 30 and 31. The detailed measurements in Figure 30 of Anderson *et al.* [73] for the $\theta_o = 60°$ case for trajectory, dilution S_{CP} and the visual width $\sqrt{2}b$ are all well predicted by the model, keeping in mind the typical mismatch between the S_{CP} and S_c values. A range of conditions for a vertical discharge $\theta_o = 90°$ was studied by Chu [74]. Some of the trajectory observations are compared in Figure 31 and illustrate the interplay of the discharge and ambient conditions that is well captured by the integral model.

A final point relates to the range of applicability of the turbulent buoyant jet dynamics in the ambient crossflow. The integral model, as well as the majority of the experimental data with a towed-source setup, assume a laminar crossflow. In actual applications the ambient unstratified flow is practically always some sort of turbulent shear flow that will incrementally interact with the turbulent flow and lead ultimately to additional erosion and break-up of the bent-over jet motion. Ultimately, a state of passive turbulent mixing plume in the ambient flow will be attained. Estimates for the end of the bent-over jet-like motions can be obtained by the equivalency of the transverse jet induced turbulent fluctuations v' to the ambient vertical fluctuation intensity w'_a,

$$v' \simeq w'_a. \tag{39}$$

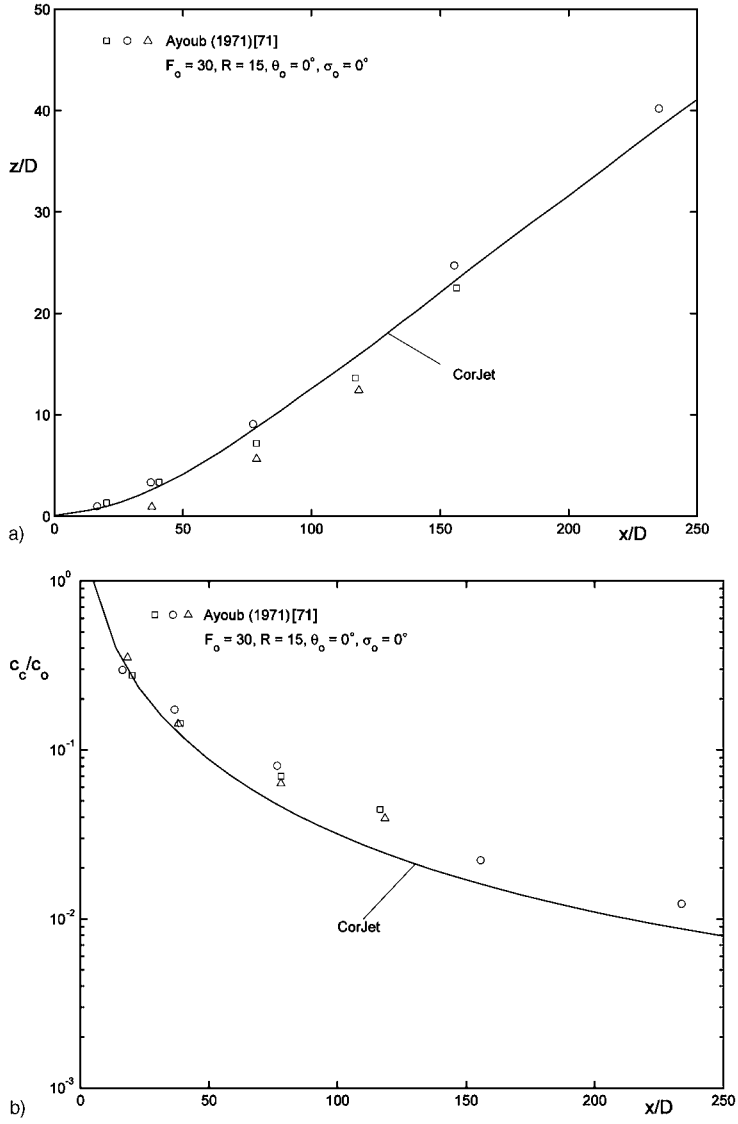

Figure 29. Horizontal buoyant jet in co-flow: Comparison of integral model predictions with laboratory data by Ayoub [71]: (a) Vertical trajectory, z/D *versus* x/D, (b) decay of normalized centerline concentration c_c/c_o as function of distance x/D.

An estimate for the first is given by $v' \simeq k_1 v_e$ in which v_e is the entrainment velocity, that for the advected regimes is simply $v_e = u_a \frac{db}{dx}$. Detailed measurements [32] suggest values of 4 to 6 for the proportionality k_1. If the ambient flow is forced by the shear stress $\tau_o = \rho_a u_*^2$ at its lower boundary, then a fluctuation intensity $w'_a \simeq k_2 u_*$ characterizes the bulk of the flow where k_2 is of order of 0.5 to 2 [75]. The shear velocity relates to the ambient velocity, $u_* = \sqrt{c_f/2}\, u_a$ with typical

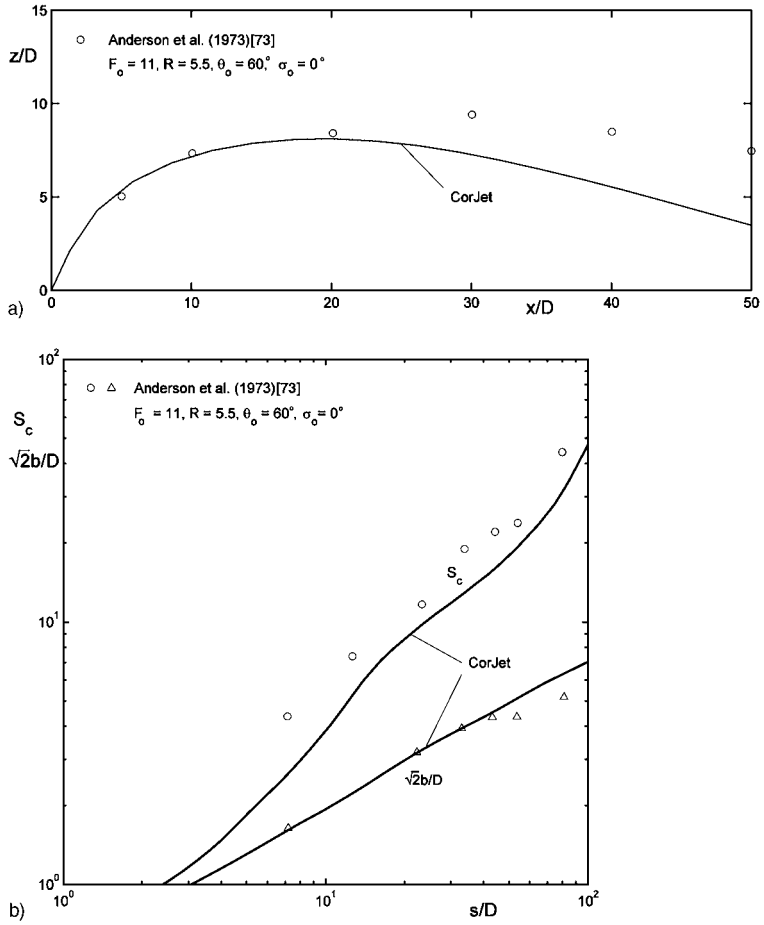

Figure 30. Negatively buoyant jet into crossflow: Comparison of integral model predictions with laboratory data by Anderson *et al.* [73]: (a) Vertical trajectory, z/D *versus* x/D, (b) centerline dilution S_c and half-velocity width $b_{1/2}/D$ as function of distance along the buoyant jet path s/D.

magnitudes for the friction coefficient c_f from 0.005 to 0.03. Upon use of these expressions Equation (39) becomes

$$k_1 \frac{db}{dx} \simeq k_2 \sqrt{\frac{c_f}{2}}. \tag{40}$$

Evaluating the growth expressions db/dx from the equations in Table I and using average coefficients $k_1 = 5$, $k_2 = 1$ and $c_f = 0.01$ leads to the these estimates for the limiting distance for momentum-induced sources

$$\frac{x_{\lim}}{L_{me}} \simeq 25, \quad \frac{x_{\lim}}{L_{mt}} \simeq 40 \tag{41}$$

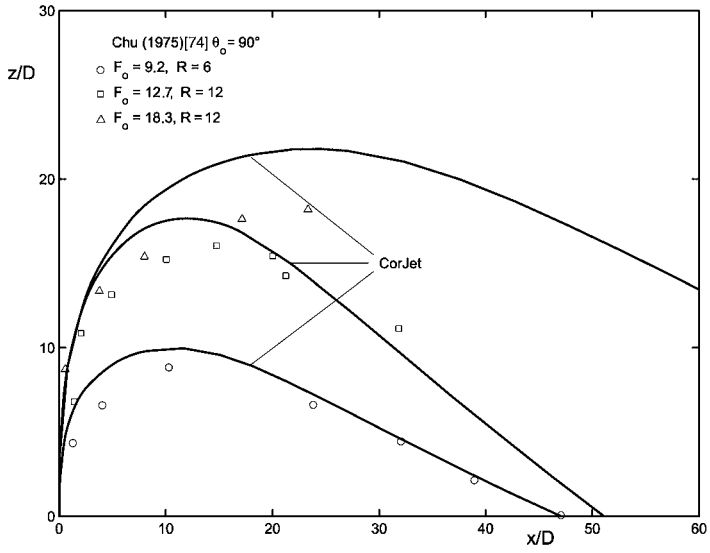

Figure 31. Negatively buoyant jets into crossflow: Comparison of integral model predictions with laboratory data by Chu [74] for two-dimensional trajectories with variable values of discharge Froude number F_o and discharge/crossflow velocity ratio R.

for the wake and advected puff regimes, respectively. The uncertainty factor for the above coefficients is about 3. The analogous estimate for the advected thermal regime yields

$$\frac{x_{\lim}}{L_b} \simeq 600 \tag{42}$$

with an uncertainty of about 10. Coincidentally, these estimates about cover the range of data reported from the towed source experiments, Figures 21 and 27, respectively. Equation (42) shows that the buoyancy-induced dynamics are considerably more efficient in maintaining a coherent turbulent plume motion in presence of ambient turbulence. This is also consistent with the fact that advected momentum sources will ultimately laminarize, as $Re_c \sim x^{-1/3}$, while for buoyancy sources the turbulence will be maintained, $Re_c \sim x^{1/3}$, in which Re_c is the local Reynolds number for the jet motion, based on width b and centerline velocity u_c or vertical rise velocity $u_a db/dx$, respectively.

4.2.3. *General Cases*

More general buoyant jet cases with three-dimensional discharge conditions or interactions with stratified crossflow involve multiple parameters and defy attempts at universal scaling.

The **buoyant jet discharging horizontally transverse into crossflow** ($|J_o| > 0$, $\theta_o = 0°$, $\sigma_o = 90°$) represents in the bending process a highly interesting case of internal vortex dynamics induced by the horizontally transverse puff motion as

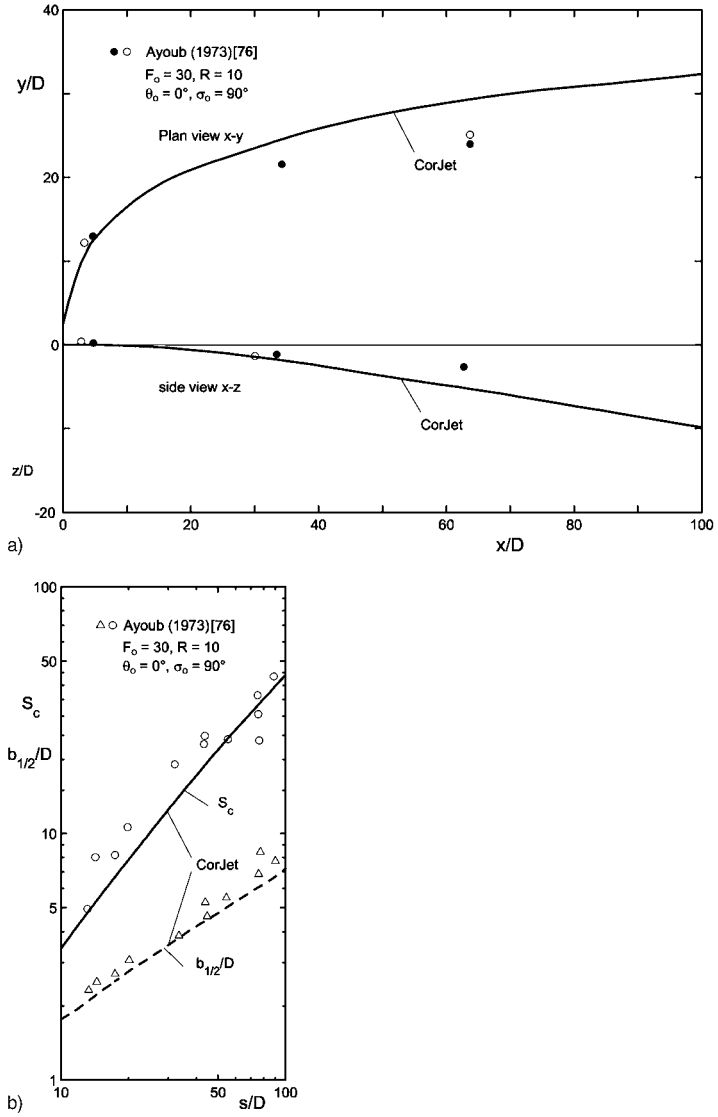

Figure 32. Buoyant jet discharging horizontally transverse into crossflow: Comparison of integral model predictions with laboratory data by Ayoub [76]: (a) Three-dimensional trajectory, y/D and z/D *versus* x/D, (b) centerline dilution S_c and half-velocity width $b_{1/2}/D$ as function of distance along the buoyant jet path s/D.

well as the vertically acting thermal. Measurements by Ayoub [76] for a negatively buoyant discharge ($J_o < 0$) are shown in Figure 32 covering the three-dimensional trajectory, the half-velocity width $b_{1/2}$ and minimum dilutions. Overall, the data, covering several test repetitions, are well predicted by the CorJet model. Some of the scatter in the dilution data is undoubtedly caused by uncertainties in sampling concentration within the variable double-vortex structure of the flow.

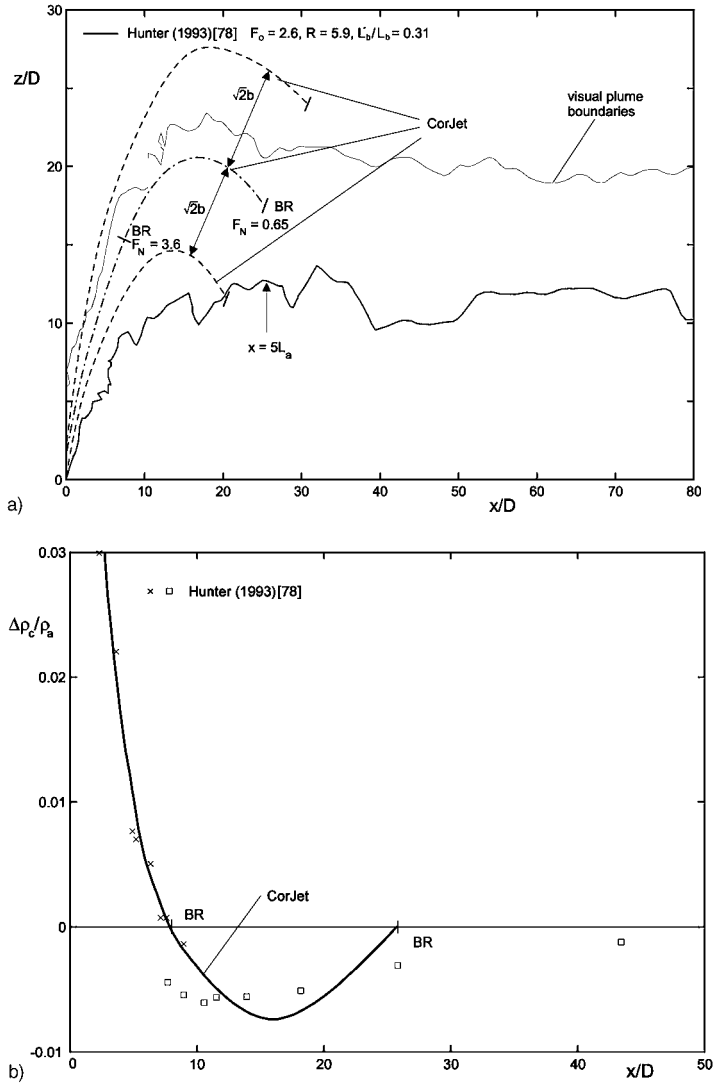

Figure 33. Vertical buoyant jet into stratified crossflow: Comparison of integral model predictions with laboratory data by Hunter [78] under weak crossflow conditions: (a) Vertical trajectory, z/D *versus* x/D, (b) centerline centerline density anomaly $\Delta\rho_c/\rho_a$ as function of downstream distance x/D. For symbols see Figure 17.

The experimental studies by Wright [77], Hunter [78] and Huq [79] were all concerned with the discharges of **vertical buoyant jets into stratified crossflow**. A multiplicity of flow conditions can occur, given the interplay of the scales listed in Equation (30) that are all relevant in this instance. In Figures 33 and 34 the integral model predictions are compared to the rather detailed measurements of Hunter that cover both the two-dimensional trajectory and the centerline density

deviation $\Delta\rho_c/\rho_a$. In both cases the initial momentum effects are limited, i.e., small values of L_M, so that the discharge buoyancy dominates. Furthermore, the cases differ as to the role of stratification relative to crossflow, as measured by the ratio L'_b/L_b. Figure 33 is a weak crossflow case (small value of $L'_b/L_b = 0.31$) in which the plume rises steeply, overshoots to a maximum trajectory height $z_{\max}$ and then settles to the equilibrium terminal level z_t. This process and the associated internal density change are well predicted. The model prediction stops at the second buoyancy reversal (transition rule 1 as proposed above) as this indicates the collapse and transition to the internal density current. The measurements by Huq for quite similar cases indicate that indeed the bulk dilution does no longer increase beyond that point. In Figure 34, on the other hand, the crossflow is much stronger (large value of $L'_b/L_b = 3.3$) leading to more rapid deflection. There is practically no overshoot and the plume finds its terminal level almost directly. In this case transition rule 2(ii) becomes effective and the plume transition is assumed at the maximum height level with a very small value of the local Froude number F_N. Practically there is a very small difference between $z_{\max}$ and $z_t$in this instance and the mismatch in the centerline density anomaly is also negligible. This transition assumption is necessary, however, as it limits the horizontal path of the jet along which more mixing would be predicted unrealistically. Clearly, there can be considerable complexities in the terminal layer formation process. But the transition rules outlined above seem to capture these reasonably well. Huq's data also indicate that the transition process seems to be complete for these buoyancy-dominated regimes at a downstream distance $x \simeq 5L_a$ where $L_a = N/u_a$ is an ambient stratified flow length scale (see Wright [77]; note also $L_a = L_b'^{4/3}/L_b^{1/3}$). This condition is also indicated in Figures 33 and 34 and seems consistent with the integral model results.

Briggs [80] first proposed an equation for the terminal level z_t of buoyancy-dominated jets in stratified crossflows from dimensional analysis that reads

$$z_t = c\, L_b^{1/3}/L_a^{2/3} = c\, L_b^{1/9}/L_b'^{8/9} \tag{43}$$

in the present length scale notation. Wright's evaluation for a large number of experiments indicate a coefficient $c = 1.85$, while analysis of Huq's and Hunter's data give a range 1.8 to 2.3. The integral model prediction cover a range 2.0 to 2.1 which include the different modes of jet collapse and transition to the internal density current.

5. Conclusions

Integral models for the analysis and prediction of turbulent buoyant jet effluxes into an ambient fluid environment are widely used in many fields of geophysical, environmental and engineering applications. The particular case of buoyant jet flows issuing into an unbounded ambient environment with uniform density or stable density stratification and under stagnant or steady sheared current conditions was

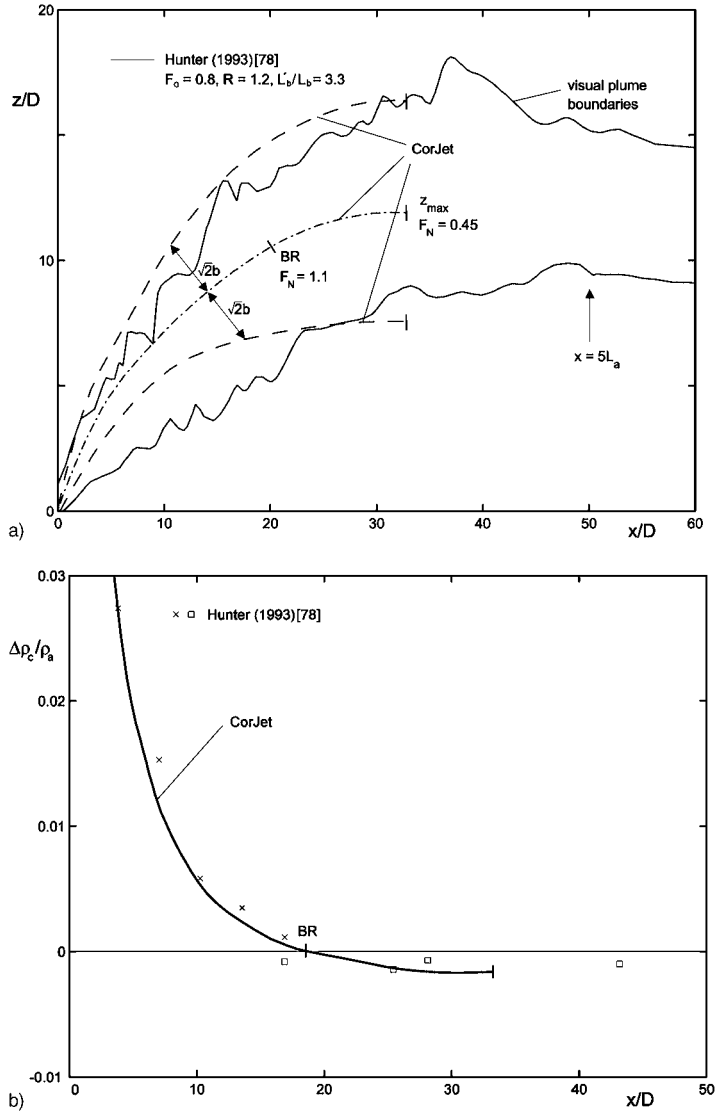

Figure 34. Vertical buoyant jet into stratified crossflow: Comparison of integral model predictions with laboratory data by Hunter [78] under strong crossflow conditions: (a) Vertical trajectory, z/D *versus* x/D, (b) centerline centerline density anomaly $\Delta\rho_c/\rho_a$ as function of downstream distance x/D. For symbols see Figure 17.

considered in this paper. The major area of application for this situation is in the analysis and design of emissions into the environment, both atmosphere and water bodies, for which reliable predictive techniques for purposes of pollution control and mitigation are needed.

The present integral model formulation for the conservation of mass, momentum, buoyancy and scalar quantities in the turbulent jet flow contains a number of im-

portant features that in aggregate make it much more general, reliable and accurate in predictive ability than earlier formulations. The model uses a three-dimensional flux-conservative formulation that minimizes singularities in the numerical integration. It defines flux quantities based on Gaussian profiles for the transverse distribution of velocity and scalars. While this profile assumption neglects the details of the distributions typical for the double-vortex structure in the final strongly bent-over stage of the buoyant jet motion, the gross features such as trajectory and minimum dilution are consistently well predicted. The model employs an entrainment closure approach that distinguishes between the five separate contributions of transverse shear (leading to jet, plume, or wake internal flow dynamics) and of azimuthal shear mechanisms (leading to advected momentum puff or thermal flow dynamics), respectively. Furthermore, the model contains a quadratic law turbulent drag force mechanism as suggested by a number of recent detailed experimental evidence on the dynamics of transverse jets into crossflow. The initial zone of flow establishment is specified with explicit account for the effects of discharge buoyancy and of crossflow on this region.

The model has been validated in several stages. First, comparison with experimental data for the five asymptotic, self-similar stages of buoyant jet flows, i.e., the pure jet, the pure plume, the pure wake, the advected line puff, and the advected line thermal, support the choice of the turbulent closure coefficients contained in the entrainment formulation. Second, comparison with many types of non-equilibrium flows support the proposed functional form of the entrainment relationship, that can be partly derived from the supplementary energy equation, but is otherwise arbitrary, and also the role of the drag force in the jet deflection dynamics. Thirdly, the range of applicability of the integral model has been carefully evaluated and a number of spatial limitations have been proposed beyond which the integral model necessarily becomes invalid. These conditions, often related to the breakdown of the boundary layer nature of the flow, describe features such as terminal layer formation in stratification, upstream penetration in jets opposing a current, or transition to passive diffusion in a turbulent ambient shear flow.

Based on the sum of these comparisons, that have focussed on parameters such as trajectories, centerline velocities, concentrations and dilutions, the model appears to provide an accurate and reliable representation of buoyant jet physics under highly general flow conditions. As such, the integral model is an convenient and efficient tool for buoyant jet analysis. Given the parabolic type of the governing differential equations, however, its major restriction lies in the assumed unboundedness of the receiving environment. Whenever, horizontal or lateral boundaries exist in the flow domain, e.g., the free surface or bottom of a water body, complex flow interactions may occur. Such resulting phenomena as jet impingement, attachment, internal hydraulic jumps, instabilities and recirculation are of course beyond the predictive powers of integral models, so that additional techniques for flow classification [46] and prediction [81] need to be considered.

Acknowledgements

The author's work for this study has been supported by grants from the U.S. Environmental Protection Agency, the U.S. National Science Foundation and the German Science Foundation (DFG). Many helpful discussions with Hannes Bühler, Rob Doneker, Joseph Lee, Hai-Jing Wang and Ian Wood are gratefully acknowledged. Thanks to Gudrun Hillebrand and Nicola Ringel who assisted with the illustrations.

Appendix A: General Formulation of the CorJet Integral Model

The integral model CorJet contains additional features beyond those described in the main text. While the jet definition diagram Figure 1 and the momentum equations, Equations (12) to (14), consider a sheared ambient velocity field $u_a(z)$, CorJet allows additionally for a skewed velocity field (e.g., Ekman spiral-type of flows) in which the ambient velocity at any level z can have a variable angle $\tau_a(z)$between the velocity vector and the x axis.

Figure A1 summarizes the local geometry. The unit vectors for the ambient current are denoted by $\vec{i}_a = (\cos\tau_a, \sin\tau_a, 0)$ and for the centerline velocity by $\vec{i}_c = (\cos\theta\cos\sigma, \cos\theta\sin\sigma, \cos\theta)$, respectively. Thus, $\vec{i}_a$ specifies directly the action of the entrainment force with components $Eu_a(\cos\tau_a, \sin\tau_a, 0)$. The drag force acts normal to the trajectory and in the $u_c - u_a$plane. Its magnitude is $|F_D| = c_D 2\sqrt{2}b\frac{u_a^2\sin^2\gamma}{2}$ and its direction is given by the unit vector $(i_x, i_y, i_z) = (\vec{i}_c \times (\vec{i}_a \times \vec{i}_c))/\sin\gamma$. Hence, the three momentum equations for the general skewed conditions are

$$\frac{d}{ds}(M\cos\theta\cos\sigma) = Eu_a\cos\tau_a + |F_D|\,i_x, \tag{A1}$$

$$\frac{d}{ds}(M\cos\theta\sin\sigma) = Eu_a\sin\tau_a + |F_D|\,i_y, \tag{A2}$$

$$\frac{d}{ds}(M\sin\theta) = \pi\lambda^2 b^2 g_c' + |F_D|\,i_z. \tag{A3}$$

CorJet also recognizes a non-conservative substance c undergoing a first-order reaction with rate constant k_d. For decay $k_d > 0$, for growth $k_d < 0$. In this case, the tracer or pollutant mass transport equation, Equation (16), modifies to

$$\frac{dQ_c}{ds} = -k_d\lambda^2\frac{Q_c}{u_{ave}} \tag{A4}$$

in which $u_{ave} = u_c\lambda^2/(1+\lambda^2) + u_a\lambda^2\cos\theta\cos(\sigma - \tau_a)$ is the tracer weighted average jet velocity (see also Appendix B).

Two types of equation of state, Equation (18), corresponding to different ambient fluids and scalar stratifying agents X_i, can be employed when using CorJet:

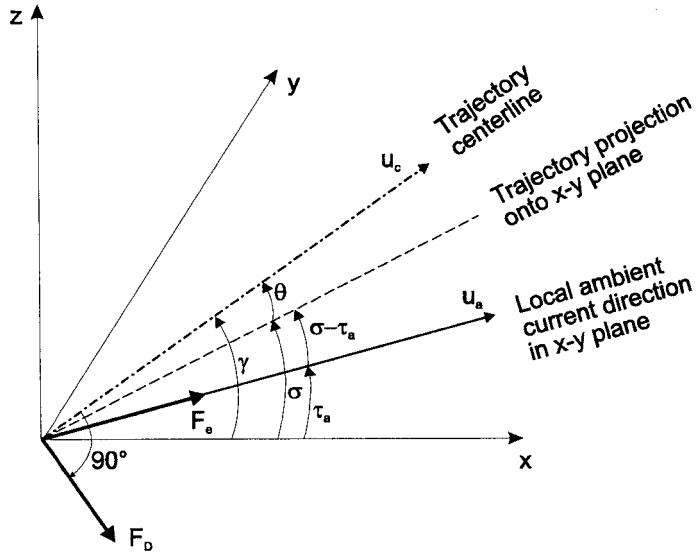

Figure A1. Local geometric relations for three-dimensional jet trajectory in skewed ambient shear flow.

(1) For temperature- and/or salinity-stratified water bodies, thus $T_a(z)$ and/or $S_a(z)$, the UNESCO (1981) equation of state is used. The fresh water density $\rho_a(T_a, 0)$ in kg/m^3 as a function of temperature T_a in °C is given by

$$\begin{aligned}\rho_a(T_a, 0) \;=\; & 999.842594 + 6.793952 \times 10^{-2} T_a - 9.095290 \times 10^{-3} T_a^2 \\ & + 1.001685 \times 10^{-4} T_a^3 - 1.120083 \times 10^{-6} T_a^4 \\ & + 6.536332 \times 10^{-9} T_a^5. \end{aligned} \tag{A5}$$

The additional effect of ambient salinity S_a in ppt (mass of dissolved solids per mass of solution times 1000) is given by

$$\begin{aligned}\rho_a(T_a, S_a) \;=\; & \rho_a(T_a, 0) + (8.24493 \times 10^{-1} - 4.0899 \times 10^{-3} T_a \\ & + 7.6438 \times 10^{-5} T_a^2 - 8.2467 \times 10^{-7} T_a^3 \\ & + 5.3875 \times 10^{-9} T_a^4) S_a + (-5.72466 \times 10^{-3} \\ & + 1.0227 \times 10^{-4} T_a - 1.6546 \times 10^{-6} T_a^2) S_a^{3/2} \\ & + 4.8314 \times 10^{-4} S_a^2. \end{aligned} \tag{A6}$$

(2) The potential density concept [95] is used for the stratified atmosphere with ambient density distribution $T_a(z)$. The potential density $\rho_a(T_a)$ in kg/m^3 of the air mass as a function of air temperature T_a in °C is

$$\rho_a(T_a) = 353.1278/(T_a + 273.15). \tag{A7}$$

The same relationships are used to calculate other density values, such as discharge density ρ_o or centerline densities ρ_c.

Appendix B: Supplemental Expressions for Local Jet Variables

Relationships for the local jet variables can be obtained from the integral (bulk) variables, Equations (6) to (10):

$$u_c = 2M/Q - 2u_a \cos\theta \cos\sigma \tag{B1}$$

$$b = Q/\sqrt{2\pi M} \tag{B2}$$

$$g_c' = J/Q_{scalar} \tag{B3}$$

$$\mathrm{X}_{ic} = Q_{\mathrm{X}i}/Q_{scalar} \tag{B4}$$

$$c_c = Q_c/Q_{scalar} \tag{B5}$$

in which $Q_{scalar} = \pi b^2 \left(u_c \lambda^2/(1+\lambda^2) + \lambda^2 u_a \cos\theta \cos\sigma\right) = \pi b^2 u_{ave}$ is the scalar weighted volume flux.

References

1. Zimm, W.: 1921, Über die Strömungsvorgänge im freien Luftstrahl, *VDI-Forschungsheft* **234**.
2. Förthmann, E.: 1934, Über turbulente Strahlausbreitung, *Ing.-Arch.* **5**, 42–54.
3. Tollmien, W.: 1926, Berechnung turbulenter Ausbreitungsvorgänge, *ZAMM* **6**, 468–478.
4. Görtler, H.: 1942, Berechnung von Aufgaben der freien Turbulenz aus Grund eines neuen Näherungsansatzes, *ZAMM* **22**, 244–254.
5. Reichardt, H.: 1942, Gesetzmäßigkeiten der freien Turbulenzen, *VDI-Forschungsheft* **414**.
6. Schmidt, W.: 1941, Turbulente Ausbreitung eines Stromes erhitzter Luft, *ZAMM* **21**, 265; 271.
7. Reichardt, H.: 1941, Über eine neue Theorie der freien Turbulenzen, *ZAMM* **21**, 257–264.
8. Albertson, J.L., Dai, Y.B., Jensen, R.A. and Rouse, H.: 1950, Diffusion of submerged jets, *Trans. ASCE* **115**, 639–664.
9. Rouse, H., Yih, C.S. and Humphreys, H.W.: 1952, Gravitational convection from a boundary source, *Tellus* **4**.
10. Morton, B.R., Taylor, G.I. and Turner, J.S.: 1956, Turbulent gravitational convection from maintained and instantaneous sources, *Proc. Roy. Soc. London* **A 234**, 1–23.
11. Morton, B.R.: 1959, Forced plumes, *J. Fluid Mech.* **5**, 151–163.
12. Turner, J.S.: 1986, Turbulent entrainment: The development of the entrainment assumption, and its application to geophysical flows, *J. Fluid Mech.* **173**, 431–471.
13. Jordinson, R.: 1956, *Flow in a Jet Directed Normal to the Wind*, R & M., No. 3974, British A.R.C.
14. Keffer, J.F. and Baines, W.D.: 1963, The round turbulent jet in a cross wind, *J. Fluid Mech.* **15**, 481–496.
15. Bryant, L.W. and Cowdrey, C.F.: 1955, The effects of velocity and temperature of discharge on the shape of smoke plumes from a tunnel or chimney. Experiments in a wind tunnel. In: *Proceedings of the Institute of Mechanical Engineering*, London, 169, pp. 371–400.
16. Scorer, R.S.: 1958, *Natural Aerodynamics*, Pergamon Press, New York.
17. Csanady, G.T.: 1961, Some observations on smoke plumes, *Int. J. Air Water Poll.* **4**, 47–51.
18. Turner, J.S.: 1960, A comparison between buoyant vortex rings and vortex pairs, *J. Fluid Mech.* **7**, 419–432.
19. Richards, R.S.: 1963, Experiment on the motion of isolated cylindrical thermals through unstratified surroundings, *Int. J. Air Water Pollut.* **7**, 17–34.
20. Abraham, G.: 1963, *Jet Diffusion in Stagnant Ambient Fluid, Delft* Hydraulics Lab., Publ. No. 29.

21. Fan, L.N.: 1967, *Turbulent Buoyant Jets into Stratified or Flowing Ambient Fluids*, Report No. KH-R-15, W.M. Keck Laboratory of Hydrology and Water Resources, California Institute of Technology, Pasadena, CA.
22. Wright, S.J.: 1977, Mean behavior of buoyant jets in a crossflow, *J. Hydraul. Div.*, *ASCE* **103**(HY5), 499–513; (5), 643–656.
23. Fischer, H.B., List, E.J., Koh, R.C.Y., Imberger, J. and Brooks, N.H: 1979, *Mixing in Inland and Coastal Waters*, Academic Press, New York, NY.
24. Frick, W.E.: 1984, Non-empirical closure of the plume equations, *Atmos. Environ.* **18**, 653–662.
25. Lee, J.H.W. and Cheung, V.: 1990, Generalized Lagrangian model for buoyant jets in current, *J. Environ. Engin.* **116**, 1085–1106.
26. Schatzmann, M.: 1978, The integral equations for round buoyant jets in stratified flows, *J. Appl. Math. Phys. (ZAMP)* **29**, 608–630.
27. Wood, I.R., Bell, R.G. and Wilkinson, D.L.: 1993, *Ocean Disposal of Wastewater*, World Scientific Publishers, Singapore.
28. Jirka, G.H. and Fong, H.L.M.: 1981, Vortex dynamics and bifurcation of buoyant jets in crossflow, *J. Engin. Mech. Div., ASCE* **107**, EM 6.
29. Chu, P.C.K.: 1996, *Mixing of Turbulent Advected Line Puffs*, Ph.D. Thesis, University of Hong Kong.
30. Hanna, S.R., Briggs, G.A. and Hosker, Jr., R.P.: 1982, *Handbook on Atmospheric Diffusion*, Technical Information Center, U.S. Department of Energy, Oak Ridge, TN.
31. List, E.J.: 1982, Mechanics of turbulent buoyant jets and plumes, In: W. Rodi (ed.), *Turbulent Jets and Buoyant Plumes*, Pergamon Press.
32. Wang, H. and Law, A.W.K.: 2002, Second-order integral model for a round buoyant jet, *J. Fluid Mech.* **459**, 397–428.
33. Fox, D.C.: 1970, Forced plume in a stratified fluid, *J. Geophys. Res.* **75**(33), 6818–6835.
34. Fric, T.F. and Roshko, A.: 1994, Vortical structure in the wake of a transverse jet, *J. Fluid Mech.* **279**, 1–47.
35. Smith, S.H. and Mungal, M.G.: 1998, Mixing, structure and scaling of the jet in crossflow, *J. Fluid Mech.* **357**, 83–122.
36. Moussa, Z.M., Trischka, J.W. and Eskinazi, S.: 1977, The near field in the mixing of a round jet with a cross-stream, *J. Fluid Mech.* **80**, 49–80.
37. Eiff, O.S. and Keffer, J.F.: 1997, On the structures in the near-wake region of an elevated turbulent jet in a crossflow, *J. Fluid Mech.* **333**, 161–195.
38. Davidson, M.J. and Pun, K.L.: 1999, Weakly advected jets in cross-flow, *J. Hydr. Engrg., ASCE* **125**, 47–58.
39. Chan, D.T.-L., Lin, J.-T. and Kennedy, J.F.: 1976, Entrainment and drag forces of deflected jets, *J. Hydraulics Div., Proc.* ASCE **102** (HY 5), 615–635.
40. Margason, R.J.: 1993, Fifty years of jet in crossflow research, *Computational and Experimental Assessment of Jets in Cross Flow*, AGARD-CP-534, Winchester, U.K.
41. Morton, B.R. and Ibbetson, A.: 1996, Jets deflected in a crossflow, *Exp. Therm. Fluid Sci.* **12**, 112–133.
42. Kelso, R.M. *et al.*: 1996, An experimental study of round jets in cross-flow, *J. Fluid Mech.* **306**, 111–144.
43. Yuan, L.L., Street, R.L. and Ferziger, J.H.: 1998, Large-eddy simulations of a round jet in crossflow, *J. Fluid Mech.* **379**, 71–104.
44. Abramovich, G.N.: 1963, *The Theory of Turbulent Jets*, The M.I.T. Press, Cambridge, MA.
45. Lee, J.H.W. and Jirka, G.H.: 1981, A vertical round buoyant jet in shallow water, *J. Hydraul. Div., ASCE* **107**, HY 12.
46. Jirka, G.H. and Doneker, R.L.: 1991, Hydrodynamic classification of submerged single port discharges, *J. Hydr. Engin.* **117**, 1095–1112.

47. Chu, P.C.K., Lee, H.H.W. and Chu, V.H.: 1999, Spreading of a turbulent round jet in coflow, *J. Hydr Engrg., ASCE* **125**, 193–204.
48. Chen, C.J. and Rodi, W.: 1980), *Vertical Buoyant Jets: A Review of Experimental Data*, Pergamon Press, Oxford.
49. Jirka, G.H. and Harleman, D.R.F.: 1979, Stability and mixing of vertical plane buoyant jet in confined depth, *J. Fluid Mech.* **94**, 275–304.
50. Nickels, T.B. and Perry, A.E.: 1996, The turbulent coflowing jet, *J. Fluid Mech.* **309**, 157–182.
51. Wang, H.-J.: 2000, *Jet Interaction in a Still or Co-Flowing Environment*, Ph.D. Thesis, Hong Kong University of Science and Technology, Hong Kong.
52. Scorer, R.S.: 1978, *Environmental Aerodynamics*, Ellis Horwood, Chichester, UK.
53. Fai, W.C.: 1991, *Advected Line Thermals and Puffs*, M. Phil. Thesis, University of Hong Kong, Hong Kong.
54. Turner, J.S.: 1966, Jets and plumes with negative or reversing buoyancy, *J. Fluid Mech.* **26**, 779–792.
55. Zhang, H. and Baddour, R.E.: 1998, Maximum penetration of vertical round dense jets at small and large Froude numbers, *J. Hydr. Engin.* **124**, 550–553.
56. Abraham, G.: 1967, Jets with negative buoyancy in homogeneous fluid, *J. Hydraulic Res.* **5**(4).
57. Roberts, P.J.W. and Toms, G.: 1987, Inclined dense jets in flowing current, *J. Hydr. Engin.* **113**, 323–341.
58. Hutter, K. and Hofer, K.: 1978, Freistrahlen im homogenen und stratifizierten Medium – ihre Theorie und deren Vergleich mit dem Experiment, *Mitteilungen der Versuchsanstalt für Wasserbau, Hydrologie und Glaziologie*, ETH Zürich, Nr. 27.
59. Roberts, P.J.W., Maile, K. and Daviero, G.: 2001, Mixing in stratified jets, *J. Hydr. Engin.* **127**, 194–200.
60. Roberts, P.J.W. and Matthews, P.R.: 1984, Dynamics of jets in two-layer stratified fluids, *J. Hydr. Engin., ASCE* **110**, 1201–1217.
61. Akar, P.J. and Jirka, G.H.: 1994, Buoyant spreading processes in pollutant transport and mixing. Part I: Lateral spreading in strong ambient current, *J. Hydraulic Res.* **32**, 815–831.
62. Jirka, G.H. and Arita, M.: 1987, Density currents or density wedges: Boundary layer influence and control methods, *J. Fluid Mech.* **177**, 186–206.
63. Baines, P.G.: 1995, *Topographic Effects in Stratified Flows*, Cambridge Monographs on Mechanics, Cambridge University Press.
64. Wong, D.R.: 1984, *Buoyant Jet Entrainment in Stratified Fluids*, Ph.D. Thesis, Civil Engineering Department, The University of Michigan, Ann Arbor, MI.
65. Pratte, B.D. and Baines, W.D.: 1967, Profiles of the round turbulent jet in a crossflow, *J. Hydr. Div., ASCE* **93**(HY6), 53–64.
66. Chu, V.H.: 1985, Oblique turbulent jets in a crossflow, *J. Eng. Mech., ASCE* **111**, 1343–1360.
67. Margason, Ri.J.: 1968, *The Path of a Jet Directed at Large Angles to a Subsonic Free Stream*, NASA TN D-4919.
68. Chan, C.H.C. and Lam, K.M.: 1998, Centreline velocity decay of a circular jet in a counterflowing stream, *Phys. Fluids* **10**, 637–644.
69. Yoda, M. and Fiedler, H.E: 1996, The round jet in a uniform counterflow: Flow visualization and mean concentration measurements, *Exp. Fluids* **21**, 427–436.
70. Cheung, V: 1991, *Mixing a Round Buoyant Jet in a Current*, Ph.D. Thesis, University of Hong Kong, Hong Kong.
71. Ayoub, G.M.: 1971, *Dispersion of Buoyant Jets in a Flowing Ambient Fluid*, Ph.D. Thesis, Imperial College, University of London.
72. Davidson, M.J., Gaskin, S. and Wood, I.R.: 2002, A study of a buoyant axisymmetric jet in a small co-flow, *J. Hydr. Res.* **40**, 477–489.

73. Anderson, J.L., Parker, F.L. and Benedict, B.A.: 1973, *Negatively Buoyant Jets in a Cross-Flow*, Environmental Protection Technology Series, U.S. Environmental Protection Agency, Washington.
74. Chu, V.H.: 1975, Turbulent dense plumes in a laminar crossflow, *J. Hydr. Res.* **13**, 263–279.
75. Nezu, I. and Nakagawa, H.: 1993, *Turbulence in Open-Channel Flows*, A.A. Balkema, Rotterdam.
76. Ayoub, G.M.: 1973, Test results on buoyant jets in injected horizontally in a cross flowing stream, *Water, Air Soil Poll.* **2**, 409.
77. Wright, S.J.: 1984, Buoyant jets in density-stratified crossflow, *J. Hydr. Engr.* **110**, (HY5), 643–656.
78. Hunter, G.C.: 1993, Experimental investigation of a buoyant jet in a stratified crossflow. In: S.D. Mobbs and J.C. King (eds.), *Waves and Turbulence in Stably Stratified Flows*, Clarendon Press, Oxford.
79. Huq, P.: 1997, Observations of jets in density stratified crossflows, *Atmos. Environ.* **31**, 2011–2022.
80. Briggs, G.A.: 1969, *Plume Rise*, U.S. Atomic Energy Commission, Division of Technical Information Extension, Oak Ridge, TN.
81. Doneker, R.L. and Jirka, G.H.: 1991, Expert systems for design and mixing zone analysis of aqueous pollutant discharges, *J. Water Resour. Plan. Manage.* **117**, 679–697.
82. Anwar, H.O.: 1972, Measurements on horizontal buoyant jets in calm ambient fluid, *La Houille Blanche* **27** (4).
83. Capp, S.P.: 1983, *Experimental Investigation of the Buoyant Axisymmetric Jet*, Ph.D. Thesis, University of Buffalo, State University of New York.
84. Cedervall, K.: 1963, *The Initial Mixing of Jet Disposal into a Recipient*, Tech. Reports 14 and 15, Div. of Hydraulics, Chalmers Institute of Technology, Goteborg, Sweden.
85. Corrsin, S. and Uberoi, M.S.: 1950, *Further Experiments on the Flow and Heat Transfer in a Heated Turbulent Air Jet*, NACA Report 998.
86. Crow, S.C. and Champagne, F.H.: 1971, Orderly structure in jet turbulence, *J. Fluid Mech* **48**, 547–596.
87. Eiff, O.S. and Keffer, J.F.: 1999, Parametric investigation of the wake-vortex lock-in for the turbulent jet discharging from a stack, *Exp. Thermal Fluid Sci.* **19**, 57–66.
88. Hansen, J. and Schroder, H.: 1968, *Horizontal Jet Dilution Studies by Use of Radiocactive Isotopes, Acta Polytechnica Scandinavia*, Civil Engineering and Building Construction Series No. 49, Copenhagen.
89. Hill, B.: 1972, Measurement of local entrainment rate in the initial region of axisymmetric turbulence air jets, *J. Fluid Mech* **51**, 773–779.
90. Hussein, H.J., Capp, S.P. and George, W.K.: 1994, Velocity measurements in a high-Reynolds-number, momentum-conserving, axisymmetric, turbulent jet, *J. Fluid Mech.* **258**, 31–75.
91. Labus, T.L. and Symons, E.P.: 1972, *Experimental Investigation of an Axisymmetric Free Jet with an Initially Uniform Velocity Profile*, NASA TN D-6783.
92. Papanicolaou, P.N. and List, W.J.: 1988, Measurement of round vertical axisymmetric buoyant jets, *J. Fluid Mech.* **195**, 341–391.
93. Ricou, F.P. and Spalding, D.B.: 1961, Measurements of entrainment by axisymmetrical turbulent jets, *J. Fluid Mech.* **11**, 21–32.
94. Rosler, R.S. and Bankoff, S.G.: 1963, Large scale turbulence characteristics of a submerged water jet, *AIChE J.* **9**, 672–676.
95. Turner, J.S.: 1973, *Buoyancy Effects in Fluids*, Cambridge University Press.